Boundary element analysis of elastic fields in non-horizontally layered halfspace whose horizontal boundary subject to tractions

S. Xiao[a], Z. Q. Yue[a,*], H.T. Xiao[b]

[a] *Department of Civil Engineering, The University of Hong Kong, Hong Kong, P. R. China*

[b] *College of Civil Engineering & Architecture, Shandong Univ. of Sci. & Tech., Qingdao, P. R. China*

Abstract

This paper presents a boundary element analysis of linear elastic fields in a layered halfspace whose material interface planes are not parallel to its horizontal boundary surface. This boundary element analysis uses the generalized Kelvin solution in a multilayered elastic solid (or the so-called Yue's solution) for taking into account the non-horizontally layered structures. It also adopts the infinite boundary elements for evaluating the influence of a far-field region. It further adopts both the discontinuous finite and infinite boundary elements to discretize the boundary surface around the strike lines of the inclined material interfaces. It uses the Kutt's numerical quadrature to evaluate the strongly singular integral in the discretized boundary integral equation. Numerical examples are presented to illustrate the effects of the non-horizontally layered materials to the displacements and stresses induced by the tractions on the horizontal boundary surface. Two non-horizontally layered halfspace models are used for numerical analysis and illustrations. Numerical results show that across the material interface, the elastic displacements are non-smoothly continuous to different degrees and some stress components can have very high values at and adjacent the interface planes, which can be important to tensile or shear failure in non-homogeneous materials.

Key words: BEM; generalized Kelvin solution; halfspace; layered solid; non-horizontal interface; infinite elements; elasticity

---

[*] Corresponding Author: Z. Q. Yue, Email: yueqzq@hku.hk, Tel: +852-28591967

1. Introduction

1.1. Horizontally layered halfspace model

Layered solid materials widely exist in nature or man-made structures. Their responses to external loadings before failure can be modelled with the responses of elastic halfspace model subject to the same external loading. The elastic halfspace model can compose of the layered elastic materials with the same mechanical properties and geometries of the actual layered solid materials. The interfaces of the layered solid materials may or may not be parallel to their boundary surfaces. Many investigations have been done for the elastic responses of the horizontally layered halfspaces subject to tractions or other types of loading conditions by many researchers since 1940s (e.g., Holl [1], Burminster [2,3,4], King [5], Singh [6] and Pan [7]). A relatively complete list of relevant publications can be found in the recent publications by Yue [8,9].

1.2. Non-horizontally layered halfspace model

As shown in Fig. 1, this paper examines the elastic responses of an elastic halfspace with non-horizontally layered solid materials due to the action of tractions at the horizontal boundary surface. There is a very limited investigation on the elastic responses of such non-horizontally layered halfspaces subject to tractions. Two examples of relevant studies are given by Pereira and Parreira [10] and Moser *et al*. [11] respectively. Due to its importance in science and engineering and its difficulties in analytical or numerical formulations, this paper aims to develop a novel boundary element method to calculate the elastic responses of the displacement and stress fields with high efficiency and accuracy.

1.3. Classical boundary element method and issues

The classical boundary element method (BEM) is ideally suited for the analysis of elastic solid materials occupying either full-space or halfspace because BEM only needs to discretize the external boundary surface and automatically satisfies the conditions at the infinity. The classical Kelvin's solution is commonly used as the fundamental singular solution in classical BEM. When it is applied to a layered solid as shown in Fig. 1, it needs to divide the layered

solid into many homogeneous domains. Furthermore, it needs to discretize the internal interfaces of the layered materials so that the continuity conditions at the internal interfaces can be formulated numerically together with those at the external boundary surfaces. For example, Pereira and Parreira [10] and Moser *et al.* [11] adopted this multi-region method of BEMs and analyzed the elastic responses of a halfspace with two non-horizontal layers subject to tractions. As the number of layers increases, however, the efficiency and accuracy of the classical BEM decrease significantly. This multi-region method also has the disadvantage in effective and accurate calculations of the elastic fields across internal material interfaces. Thirdly, the fundamental singular solutions, used as the kernel functions, in the classical BEMs vary rapidly if an internal point is very close to the elements located at material interfaces.

1.4. Aim and approach of this study

In this paper, a single-region BEM is developed and presented for the analysis of the elastic responses of a non-horizontally layered halfspace subject to tractions (Fig. 1). The generalized Kelvin solution in a multilayered elastic solid given by Yue [12] is used to eliminate the discretization task at the internal interfaces of layered materials. Furthermore, the infinite boundary element technique proposed by Moser *et al.* [11] is used to take into account the influence of a far-field region because of its straightforward implementation. Other infinite boundary element techniques can be found in the publications by Waston [13], Beer *et al.* [14], Beer and Waston [15], Zhang *et al.* [16], Liu and Farris [17], Pereira and Parreira [10], Davies *et al.* [18], Bu [19], Gao and Davies [20], Moser *et al.* [11], Salvadori [21], Liang and Liew [22] and Ribeiro *et al.* [23]. Thirdly, the discontinuous boundary element technique is adopted to deal with the step-discontinuity of material properties at the interface strike line on the horizontal boundary surface of the non-horizontally layered halfspace. Fourthly, special attentions are given to various singular integrals involved in the discretized boundary integral equations. The proposed BEM is applied to specifically solving the elastic response of a halfspace with two or three non-horizontal layers under a square footing loading on the horizontal boundary surface. Numerical results show the influence of non-horizontally

layered materials to the elastic displacement and stress fields induced by the normal footing tractions on the horizontal boundary surface.

2. The governing equations for BEM in non-horizontally layered halfspace

Fig. 2 shows the horizontally oriented boundary surface of the non-horizontally layered halfspace model. The interface strike line represents an intersection line of an internal interface plane of any two fully contacted dissimilar material layers with the horizontal boundary surface. The boundary surface is divided into two parts S_F and S_I. They represent a core region around the traction area and a far-field region beyond the traction area, respectively. Accordingly, using the generalized Kelvin solution of a multilayered solid occupying the full-space [12], the boundary integral equations for the non-horizontally layered halfspace without body forces can be expressed as

$$c_{ij}(P)\, u_j(P) + \int_{S_F+S_I} t_{ij}^Y(P,Q) u_j(Q) dS(Q) = \int_{S_F+S_I} u_{ij}^Y(P,Q) t_j(Q) dS(Q) \tag{1}$$

where P and Q are, respectively, the field and source points; t_j and u_j are, respectively, tractions and displacement; t_{ij}^Y and u_{ij}^Y are, respectively, the kernel functions of the tractions and displacements of the generalized Kelvin solution.

The free term $c_{ij}(P)$ in Eq. (1) depends only upon the asymmetric behavior of the singular terms of the generalized Kelvin solution and the local geometry of the boundary at the point P. In using the fundamental solution of a layered space, $c_{ij}(P) = 0.5\delta_{ij}$ for the point P located on a smooth boundary and not at the material interface [24]. When the point P is located at the strike line of the material interface on the horizontal boundary surface, there is no closed-form expression for $c_{ij}(P)$ available in the open literature. So, instead, the discontinuous boundary element technique is adopted for resolving this task. Its details are given in Section 4.1.

After obtaining the displacements and tractions on the boundary, the displacements at any internal point p can be determined by using the displacement integral equations as follows

$$u_i(p) + \int_{S_F+S_I} t_{ij}^Y(p,Q) u_j(Q) dS(Q) = \int_{S_F+S_I} u_{ij}^Y(p,Q) t_j(Q) dS(Q) \tag{2}$$

By using Eq. (2), the strain-displacement equations and the constitutive equations, the stresses at any internal point p can be expressed as

$$\sigma_{ij}(p) = \int_{S_F+S_I} U_{ijk}^Y(p,Q)t_k(Q)dS(Q) - \int_{S_F+S_I} T_{ijk}^Y(p,Q)u_k(Q)dS(Q) \tag{3}$$

where U_{ijk}^Y and T_{ijk}^Y are the new kernel functions obtained from the displacements and stresses of the generalized Kelvin solution in a layered solid of full-space extent and the relative functions are presented in Appendix A.

3. The generalized Kelvin solution in non-horizontally layered fullspace

3.1. Two Cartesian coordinate systems and relationship

As shown in Figs. 1 and 2, the boundary integral equations are established in the Cartesian coordinate system $Oxyz$, where the non-horizontally layered material interface planes have a dip angle θ to the horizontal xy plane. On the other hand, another Cartesian coordinate system $O'x'y'z'$, shown in Fig. 3, is used for calculating the displacements and stresses of the generalized Kelvin solution, where the $O'x'y'$ plane is parallel and the z axis is perpendicular to the non-horizontally layered material interface planes. The y and y' axes of the two Cartesian coordinate systems are parallel to each other.

3.2. The generalized Kelvin solution in $O'x'y'z'$ and $Oxyz$ coordinates

As shown in Fig. 3, the generalized Kelvin solution (i.e., the kernel functions in Eqs. (1)-(3)) is presented in the Cartesian coordinate system $O'x'y'z'$. The solution was given by Yue [12] for the elastic response of a n-layered solid of full-space extent subject to a point body force vector $(f_{x'}, f_{y'}, f_{z'})$ at any point in the interior of the layered solid. More details of the solution and its mathematical formulation and verification can be found in Yue [8,9]. The solution given by Yue [8,9,25] is re-named as Yue's solution by Merkel et al. [26] and Maloney et al. [27] in their analysis of the stresses and deformation induced in cells.

Since 2000, Yue and his co-workers [28] have incorporated this generalized Kelvin solution into the classical BEMs for the analysis of the fracture mechanics in layered solids and found

the solutions for many specific problems of interests in science and technology, where the layered material interface planes are horizontally placed and parallel to the horizontal boundary surface. In this paper, we attempt to extend the BEMs for the elastic analysis of displacement and stress fields in the non-horizontally layered halfspace due to tractions on the horizontal boundary surface.

For an ease of reference, some basic formulations of the fundamental solution are provided in Appendix B. It is the analytical solution of closed-form singularity terms for the elastostatic field in a layered solid of full-space extent due to the action of a point force vector (Fig. 3). The total number of the dissimilar layers is an arbitrary nonnegative integer n. The dissimilar homogeneous layers adhere an elastic solid of upper halfspace extent and another elastic solid of lower halfspace extent. The interface between any two connected dissimilar layers is fully bonded.

As shown in Fig. 4, the generalized Kelvin solution (i.e., the displacements $u_{i'}$ and stresses $\sigma_{i'j'}$) due to the point force vector $\left(f_x, f_y, f_z\right)$ in the Cartesian coordinate system $Oxyz$ can be obtained from those due to the point force vector $\left(f_{x'}, f_{y'}, f_{z'}\right)$ in the Cartesian coordinate system $O'x'y'z'$. Detailed descriptions are presented in Appendix C.

4. Five boundary element techniques for BEM in non-horizontally layered halfspace

4.1. General

As shown in Fig. 2, the horizontal boundary surface $(-\infty < x, y < +\infty,\ z = 0)$ can be divided into two regions S_F and S_I. Each region can be further divided into two sub-areas. The first sub-area has homogeneous material properties and is away from the material interface strike line. The second sub-area has step-discontinuous in material properties along the x-axis across the strike line and covers or adjacent to the strike line. So, the entire horizontal boundary surface has to be divided into four types of boundary areas: finite homogeneous area, finite area with strike line, infinite homogeneous area, and infinite area with strike line.

The free term $c_{ij}(P)$ depends on the shape of the boundary and/or elastic parameters. The closed-form expression of $c_{ij}(P)$ is not available for the point P located on an interface strike line where the two elastic parameters are step-discontinuous along the x-axis direction on the boundary surface. Secondly, if the nodes of a continuous boundary element are not located on the interface strike line, the line can be covered by the element. For this situation, the Kutt's numerical quadrature presented in Section 5 below cannot be used to calculate the strongly singular integral of the BEM. Thirdly, when the tractions of a node on the interface strike line are unknown, a step-discontinuity in the traction can occur at that node, which implies that the number of equations at that node is smaller than the number of unknowns at that node. Hence, the following discontinuous boundary element technique is adopted to numerically resolve this task for BEM in non-horizontally layered halfspace. Accordingly, the following five boundary element techniques are used.

4.2. Continuous finite element for homogenous boundary area (type I)

The conventional eight-node isoparametric and continuous elements which are introduced by Xiao and Yue [28] are shown in Fig. 5a. They are employed to discretize the finite core region S_F that is homogeneous in material properties and away from the material interface strike lines. The coordinates at any point in a finite boundary element can be related to its element nodal values as follows:

$$\boldsymbol{x} = \boldsymbol{N}\boldsymbol{x}^e \tag{11a}$$

where $\boldsymbol{x}\,(=\begin{bmatrix} x & y & z \end{bmatrix}^{\mathrm{T}})$ are Cartesian coordinates of the point with intrinsic coordinates (ξ, η), $\boldsymbol{x}^e\,(=\begin{bmatrix} \boldsymbol{x}_1^{\mathrm{T}} & \boldsymbol{x}_2^{\mathrm{T}} & \cdots & \boldsymbol{x}_8^{\mathrm{T}} \end{bmatrix}^{\mathrm{T}})$ is a vector containing coordinates of nodal points at element e and $\boldsymbol{N}\,(=\begin{bmatrix} N_1\boldsymbol{I}_3 & N_2\boldsymbol{I}_3 & \cdots & N_8\boldsymbol{I}_3 \end{bmatrix})$ is a matrix of the shape functions of a continuous finite element listed in Appendix D.1 ($\boldsymbol{I}_3$ is a unit matrix (3×3)).

In a finite boundary element, the displacements and tractions are approximated using the following representation:

$$\boldsymbol{u} = \boldsymbol{N}\boldsymbol{u}^e \tag{11b}$$

$$t = Nt^e \tag{11c}$$

where $\boldsymbol{u}$ $(=\begin{bmatrix} u_x & u_y & u_z \end{bmatrix}^{\mathrm{T}})$ and $\boldsymbol{t}$ $(=\begin{bmatrix} t_x & t_y & t_z \end{bmatrix}^{\mathrm{T}})$ are, respectively, the displacements and tractions of the point with intrinsic coordinates (ξ, η) and $\boldsymbol{u}^e$ $(=\begin{bmatrix} \boldsymbol{u}_1^{\mathrm{T}} & \boldsymbol{u}_2^{\mathrm{T}} & \cdots & \boldsymbol{u}_8^{\mathrm{T}} \end{bmatrix}^{\mathrm{T}})$ and $\boldsymbol{t}^e$ $(=\begin{bmatrix} \boldsymbol{t}_1^{\mathrm{T}} & \boldsymbol{t}_2^{\mathrm{T}} & \cdots & \boldsymbol{t}_8^{\mathrm{T}} \end{bmatrix}^{\mathrm{T}})$ are, respectively, vectors containing displacements and tractions of nodal points at element e.

4.3. Discontinuous finite element for boundary area with interface strike line (type II)

The eight-node isoparametric and discontinuous elements (type II), shown in Fig. 5b, are employed to discretize the finite area with strike line on the region S_F. The element type II is positioned on two sides of the material interface strike line. Comparing to the element type I, the nodes 1, 2 and 5 of the discontinuous element are moved inside to avoid the discontinuities of unknown tractions and the traction kernel. The shape functions of the element type II are listed in Appendix D.2 where the discontinuous nodes are at a distance of 1/3 from the element edge $\eta = -1$. The coordinates, displacements and stresses at any point in a finite boundary element can be related to its element nodal values by using Eqs. (11a)-(11c).

4.4. Continuous infinite element for homogenous boundary area (type III)

In order to consider the influence of a far field, the continuous infinite element developed by Moser *et al*. [11], as shown in Fig. 6a, is employed to the infinite region S_I that is homogeneous in material properties and away from the material interface strike line. The coordinates at any point in an infinite element is then related to its element nodal coordinates as follows:

$$x = {}^{\infty}Nx^e \tag{12a}$$

where ${}^{\infty}N$ $(=\begin{bmatrix} {}^{\infty}N_1\mathbf{I}_3 & {}^{\infty}N_2\mathbf{I}_3 & \cdots & {}^{\infty}N_6\mathbf{I}_3 \end{bmatrix})$ is a matrix of the shape functions of an infinite element listed in Appendix D.3 ($\mathbf{I}_3$ is a unit matrix (3×3)).

In an infinite boundary element, the displacements and tractions are approximated using the following representation:

$$u = {}^{\infty}\!N^u u^e \tag{12b}$$

$$t = {}^{\infty}\!N^t t^e \tag{12c}$$

where ${}^{\infty}\!N^u \left(= \begin{bmatrix} {}^{\infty}\!N_1^u \mathbf{I}_3 & {}^{\infty}\!N_2^u \mathbf{I}_3 & \cdots & {}^{\infty}\!N_6^u \mathbf{I}_3 \end{bmatrix}\right)$ and ${}^{\infty}\!N^t \left(= \begin{bmatrix} {}^{\infty}\!N_1^t \mathbf{I}_3 & {}^{\infty}\!N_2^t \mathbf{I}_3 & \cdots & {}^{\infty}\!N_6^t \mathbf{I}_3 \end{bmatrix}\right)$ are, respectively, matrices of the interpolation functions of displacements and tractions listed in Appendix D.3 ($\mathbf{I}_3$ is a unit matrix (3×3)).

4.5. Discontinuous infinite element for boundary area with interface strike line (type IV)

The discontinuous infinite elements (type IV), shown in Fig. 6b, are employed to discretize the infinite area with strike line on the region S_I. Comparing to the element type III, the nodes 1 and 4 of the discontinuous element are moved inside to avoid the discontinuity of the traction kernel. The shape functions and interpolation functions of the element type IV are listed in Appendix D.4 where the discontinuous nodes are at a distance of 1/3 from the element edge $\xi = -1$. The coordinates, displacements and stresses at any point in an infinite boundary element can be related to its element nodal values by using Eqs. (12a)-(12c).

4.6. Discontinuous infinite element for boundary area with interface strike line (type V)

The discontinuous infinite elements (type V), shown in Fig. 6c, are also employed to discretize the infinite area with strike line on the region S_I. Comparing to the element type III, the nodes 2 and 3 of the discontinuous element are moved inside to avoid the discontinuity of the traction kernel. The shape functions and interpolation functions of the element type V are listed in Appendix D.5 where the discontinuous nodes are at a distance of 1/3 from the element edge $\xi = 1$. The shape functions and interpolation functions are different from those of elements (type IV) and substituting these functions of the element type V into Eqs. (12a)-(12c), the coordinates, displacements and tractions at any point in the element type V can be related to its element nodal values.

5. Numerical integrations for BEM in non-horizontally layered halfspace

5.1. Discretized governing boundary integral equations

The above five boundary elements are used for discretization of the horizontal boundary surface S_F and S_I. The governing boundary integral equation (1) can be re-written as the following discretized expressions

$$c_{ij}(P)u_j(P)+\sum_{e=1}^{FBE}\int_{S_F^e}t_{ij}^Y(P,Q)u_j(Q)dS(Q)+\sum_{e=1}^{IBE}\int_{S_I^e}t_{ij}^Y(P,Q)u_j(Q)dS(Q)$$

$$=\sum_{e=1}^{FBE}\int_{S_F^e}u_{ij}^Y(P,Q)t_j(Q)dS(Q)+\sum_{e=1}^{IBE}\int_{S_I^e}u_{ij}^Y(P,Q)t_j(Q)dS(Q)$$

(13)

where *FBE* and *IBE* are the numbers of finite and infinite boundary elements, respectively.

Using Eqs. (11) and (12), Eq. (13) can be further re-written as follows:

$$c_{ij}(P)u_j(P)+\sum_{e=1}^{FBE}\sum_{\alpha=1}^{8}u_j^\alpha(Q^\alpha)\int_{S_F^e}t_{ij}^Y(P,Q)N_\alpha dS(Q)+\sum_{e=1}^{IBE}\sum_{\alpha=1}^{6}u_j^\alpha(Q^\alpha)\int_{S_I^e}t_{ij}^Y(P,Q)^\infty N_\alpha^u dS(Q)$$

$$=\sum_{e=1}^{FBE}\sum_{\alpha=1}^{8}t_j^\alpha(Q^\alpha)\int_{S_F^e}u_{ij}^Y(P,Q)N_\alpha dS(Q)+\sum_{e=1}^{IBE}\sum_{\alpha=1}^{6}t_j^\alpha(Q^\alpha)\int_{S_I^e}u_{ij}^Y(P,Q)^\infty N_\alpha^t dS(Q)$$

(14)

The coefficients of the displacements and tractions at all the nodes in Eq. (14) are first calculated with numerical integration techniques. A set of linear algebraic equations is then formed for the determination of all boundary unknowns of displacements and tractions at the nodes. The generalized minimum residual algorithm is adopted in solving the set of linear algebraic equations, which can reduce the calculation time.

5.2. Numerical techniques for regular and weakly singular integrals

In Eq. (14), when the source point *P* is not collocated on an integration element within either S_F^e or S_I^e, all the integrals are regular. These regular integrals can be evaluated using the Gaussian quadrature rule. When the source point *P* is located in the same boundary element as the field point *Q* and $P=Q^\alpha$, both weakly and strongly singular integrals exist. An element subdivision technique developed by Lachat and Watson [29] is used to calculate the weakly singular integrals. The strongly singular integrals are evaluated using the numerical method described in Section 5.3.

After the unknown displacements and tractions at the nodes are determined from Eq. (14), the discretized equations (2) and (3) do not contain unknown variables. Because the internal point *p* under consideration is located within the domain, the singular integrals in Eqs. (2) and

(3) do not exist. Thus, the traditional Gaussian quadrature can be directly used for calculating the displacements and stresses at any internal point. When the internal point p is very close to the integration region on the boundary surface, the kernels in Eqs. (2) and (3) can vary rapidly. To obtain the desired accuracy of such integrals, an effective method is to implement a scheme of subdividing the element into sub-regions of integration. The subdivision scheme in Beer *et al.* [30] and Gao and Davies [31] are adopted in the present BEM.

5.3. Numerical techniques for strongly singular integrals

5.3.1 General

Since infinite boundary elements are used in this BEM, the strongly singular integrals cannot be evaluated indirectly using the rigid displacement method. Beer and Watson [14] evaluated the strongly singular integrals indirectly through the computation of an azimuthal integral, which is not an easy task. Pereira and Parreira [10] and Moser *et al.* [11] used the method proposed by Guiggiani and Gigante [32] to directly evaluate the strongly singular integrals. More recently, Gao [33] and Gao *et al.* [34] analytically evaluated all kinds of singular boundary integrals in 2D/3D BEM analysis. However, this direct method may not be applicable to the BEM of fundamental solutions with complex functions. If a numerical quadrature can be used directly for the evaluation of strongly singular integrals, the implementation of infinite boundary elements becomes a straightforward task.

5.3.2 Kutt's numerical quadrature

A Kutt's numerical quadrature is adopted to calculate the strongly singular integrals for the infinite and finite elements, shown in Figs. 5 and 6. Here, the proposed numerical quadrature is presented only for the continuous infinite element (type III), shown in Fig. 6a and, of course, is easily used to other types of boundary elements, as shown in Figs. 5 and 6. On an infinite boundary element, the strongly singular integral can be expressed as

$$\int_{-1}^{1}\int_{-1}^{1} t_{ij}^{Y} \left[P(\xi^{c}, \eta^{c}), Q(\xi, \eta) \right]^{\infty} N_{\alpha}^{u}(\xi, \eta) J(\xi, \eta) d\xi d\eta \tag{15}$$

where J is the Jacobian transformation. The collocation point $P(\xi^{c}, \eta^{c})$ in Eq. (15) coincides with one of the nodal points on the element.

Following Pan and Yuan [35], the strongly singular integral (15) can also be calculated by using the numerical quadrature proposed by Kutt [36,37]. Introducing the following polar point at the source point P on the element

$$\xi = \xi^c + r\cos\theta \quad \text{and} \quad \eta = \eta^c + r\sin\theta \tag{16}$$

Eq. (15) can then be written as

$$\sum_m \int_{\theta_1}^{\theta_2} \int_0^{R(\theta)} t_{ij}^Y \left[P\left(\xi^c, \eta^c\right), Q(r, \theta) \right]^\infty N_\alpha^u (r, \theta) J(r, \theta) r \, dr \, d\theta \tag{17}$$

where the summation on m is for all the triangles on the element.

These triangles are formed by connecting the source point and two corners. In the ensuing, we present this subdivision technique for a continuous infinite boundary element, as shown in Fig. 7. The details are further given below on the basis of three locations of the collocation point.

Location a) (Fig. 7a)

If the collocation point is located at the corner node 1 of the element, the element is then divided into two triangles and the summation on m in Eq. (17) is from 1 to 2. As shown in Fig. 7a, $\left(\xi^c, \eta^c\right) = (-1, -1)$. Eq. (16) can be re-written as $\xi = -1 + r\cos\theta$ and $\eta = -1 + r\sin\theta$. For the triangle 1, $\theta \in [0, \pi/4]$ and $R(\theta) = 2/\cos\theta$; for the triangle 2, $\theta \in [\pi/4, \pi/2]$ and $R(\theta) = 2/\cos(\theta - \pi/2)$.

Location b) (Fig. 7b)

If the collocation point is located at the corner node 2, the element needs to be divided into two triangles, and the summation on m in Eq. (17) is from 1 to 2. As shown in Fig. 7b, $\left(\xi^c, \eta^c\right) = (1, -1)$. Eq. (16) can be re-written as $\xi = 1 + r\cos\theta$ and $\eta = -1 + r\sin\theta$. For the triangle 1, $\theta \in [\pi/2, 3\pi/4]$ and $R(\theta) = 2/\cos(\theta - \pi/2)$; for the triangle 2, $\theta \in [3\pi/4, \pi]$ and $R(\theta) = 2/\cos(\pi - \theta)$.

Location c) (Fig. 7c)

If the collocation point is located at the middle node 5 of the square side, the element needs to be divided into three triangles, and the summation on m in Eq. (17) is from 1 to 3. As shown in in Fig. 7c, $\left(\xi^c, \eta^c\right) = (0, -1)$. Eq. (16) can be re-written as $\xi = r\cos\theta$ and $\eta = -1 + r\sin\theta$. For different triangles, there are the following integral parameters:

- For the triangle 1, $\theta \in \left[0, \mathrm{atan}(2)\right]$ and $R(\theta) = 1/\cos\theta$;

- For the triangle 2, $\theta \in \left[\mathrm{atan}(2), \pi - \mathrm{atan}(2)\right]$ and $R(\theta) = 2/\cos(\theta - \pi/2)$;

- For the triangle 3, $\theta \in \left[\pi/2 - \mathrm{atan}(2), \pi\right]$ and $R(\theta) = 1/\cos(\pi - \theta)$.

From Eq. (17), it is observed that the integrand is $O(1/r)$, where r is the distance between the source and field points. Therefore, the Kutt's numerical quadrature can be utilized to evaluate the inner finite-part integral-part integral with respect to r. The outer integral with respect to θ is regular and can be calculated with the regular Gauss quadrature. For a given Gauss point θ_j, the inner integral in Eq. (17) can be approximated with Kutt's N-point equispace quadrature as follows

$$\int_0^R \frac{f(r)}{r} dr \approx \sum_{l=1}^N (w_l + c_l \, ln \, R) f\left(\frac{l-1}{N}R\right) \tag{18}$$

where w_l are the weights and c_l is the coefficients given by Kutt, and the integrand is given by

$$f(r) = t_{ij}^Y \left[P\left(\xi^c, \eta^c\right), Q\left(r, \theta_j\right)\right] {}^\infty N_\alpha^u\left(r, \theta_j\right) J\left(r, \theta_j\right) r^2 \tag{19}$$

In applying Kutt's N-point equispace quadrature (18), it is assumed that the integrand $f(r) \in C^0[0, R]$ and $f(r) \in C^1$ in the neighborhood of $r = 0$. In discretizing the boundary surface, discontinuous finite and infinite elements are positioned on the two sides of the material interface strike line. In this case, the integrand $f(r)$ in Eq. (19) is smoothly continuous for the domain $[0, R]$ and the quadrature (18) is used for evaluating the integral (17). In the following numerical examples, the Kutt's 20-point equispace quadrature is used in

the finite-part integral with respect to r, and 20 Gaussian points for the regular outer integral with respect to θ_j.

6. Numerical verifications

Based on the above analytical and numerical equations, the BEM program in Fortran is made to calculate the elastostatic fields of displacements and stresses in a non-horizontally layered halfspace. This BEM program can calculate all the field variables at any point in a non-homogeneous layered halfspace induced by different tractions on the horizontal boundary surface. This section presents the numerical results of two elastic halfspace models to verify the present BEM program.

6.1. Square footing on a homogeneous halfspace (example 1)

This example in Moser *et al*. [11] is used to verify the present BEM program. The elastic halfspace has the modulus of 10000 kN/m^2 and a zero Possion's ratio. A pressure of 100 kN/m^2 uniformly acts on a square area with the side length of 2 m on the horizontal boundary surface of the elastic halfspace. The boundary element mesh given in Fig. 4 of Moser *et al*. [11] is used. The present BEM program gives the vertical displacements of 0.022785 and 0.011379 m at the center and the corner of the loaded square area, respectively. The exact vertical displacements at these two points are 0.022444 and 0.011222 m, respectively. The maximum relative difference between the present numerical results and the exact results is 1.52%.

6.2. Square footing on a bi-material halfspace with non-horizontal interface (example 2)

The example in Pereira and Parreira [10] is also used to verify the present BEM program. As shown in Fig. 8, an elastic halfspace has two different materials that are fully bonded at their non-horizontal interface. The dip angle of the non-horizontal interface plane is 45° ($\pi/4$). The strike line of the inclined material interface plane with the horizontal boundary surface is located at the line of $x = 1.5$ m, $-\infty < y < +\infty$ and z=0. A square area (1 m × 1 m) of its horizontal boundary surface is subject to a uniformly distributed footing pressure of 100 kN/m^2. The elastic moduli of the two materials are, respectively, 10000 and 2000 kN/m^2. The

values of both materials' Poisson's ratios are zero.

As shown in Fig. 9, the core region S_F is represented by a square area (5 m × 5 m) covering the loaded square area (1 m × 1 m). The center of the square core region S_F is identical to the center of the loaded square area. The square core region is further divided into the first and second sub-areas. The first sub-area is not adjacent to the interface strike line and is discretized with a total of 284 finite continuous elements (type I). The second sub-area is on both sides of the interface strike line and is discretized with a total of 36 (2×18) finite discontinuous elements (type II). The far-field region S_I outside the square core region is also further divided into the third and fourth sub-areas. The third sub-area is not adjacent to the interface strike line and is discretized with a total of 60 infinite continuous elements (type III). The fourth sub-area is on both sides of the interface strike line. Both side areas are discretized with one infinite discontinuous element (type IV) and one infinite discontinuous element (type V). The discontinuous elements are positioned on the narrow left and right side areas adjacent the interface strike line.

The present BEM program gives the vertical displacement values of 0.022900, 0.011405 and 0.011233 m at the center, the two corners nearer to the interface and the other two corners of loaded square area, respectively. Because of symmetry, the vertical displacements at the two corners ($x = 1$ m, $y = \pm 1$ m, $z = 0$) are the same. The corresponding values presented by Pereira and Parreira [10] are 0.022428, 0.011216 and 0.011195 m, respectively. The maximum relative difference between these two BEM programs is 2.1%. Pereira and Parreira [10] used the classical Kelvin's solution based BEM program where the inclined interface plane is discretized with elements. The present BEM does not need to discretize the inclined interface plane.

7. Numerical examples

7.1. Square footing on bi-material halfspace with one non-horizontal interface

7.1.1 General

This elastostatic problem is shown in Fig. 10. It is similar to the elastostatic problem examined in Section 6.2 and by Pereira and Parreira [10] (Fig. 8). The non-horizontal

bi-material interface dips at the arbitrary angle θ with the horizontal boundary surface. Its strike line is exactly along the *y*-axis. The bi-materials have their elastic properties as follows: E_1=20 GPa, $v_1 = 0.3$, E_2=40 GPa, and $v_2 = 0.25$. The square loading area has a side length of 2 m and is acted by a uniformly distributed pressure of 100 MPa. The adopted boundary element meshes are much similar to the meshes shown in Fig. 9. The discontinuous elements are positioned on the two narrow zones on both sides of the material interface strike line (i.e., the *y*-axis). The two locations (noted as *a* and *b* in Fig. 10) correspond to $(x = -1 \text{ m}, z = 0)$ and $(x = 1 \text{ m}, z = 0)$, respectively. The symbol c' is the horizontal distance from the point *c* on the material interface to the vertical coordinate plane $(x = 0, \ -\infty < y, z < +\infty)$. The c' values are equal to 1.7321, 0.5774, 0, -0.5774 and -1.7321 m, respectively for θ= 30°, 60°, 90°, 120° and 150°. For benchmarking of the numerical results, the elastostatic problems of the homogeneous halfspace with either the material 1 (E_1=20 GPa and $v_1 = 0.3$) or the material 2 (E_2=40 GPa and $v_2 = 0.25$) under the same pressure loading are also calculated and presented below.

7.1.2 Variations of elastic fields with x-axis for different θ values

Fig. 11 shows the variations of the three displacements (u_x, u_y, u_z) along $-5 \text{ m} \leq x \leq 5 \text{ m}$ at (*y* = 0.5 m and *z* = 1 m) for the dip angle θ value of 30°, 60°, 90°, 120°, or 150°. It is evident that (1) the u_x in a homogeneous elastic halfspace shows an anti-symmetrical distribution about the vertical coordinate plane $(x = 0, \ -\infty < y, z < +\infty)$ and (2) the u_y and u_z in a homogeneous elastic halfspace shows a symmetrical distribution about the vertical coordinate plane. However, the (u_x, u_y, u_z) in the bi-material elastic halfspace do not have such anti-symmetrical or symmetrical distributions. The u_z (or u_y) value in the bi-material halfspace for each θ value is almost bonded by the two corresponding u_z (or u_y) values in the two homogeneous elastic halfspaces. But, the u_x value in the bi-material halfspace can

be either larger or less than the two corresponding u_x values in the two homogeneous elastic halfspaces. The u_x in the bi-material halfspace increases as θ increases from 30° to 90° and decreases as θ increases from $90°$ to $150°$. The u_y and u_z in the bi-material halfspace increase as θ increases from $30°$ to $150°$. Such results are due to the fact that as θ increases, the softer material 1 (E_1=20 GPa and $v_1 = 0.3$) is enlarged whilst the harder material 2 (E_2=40 GPa and $v_2 = 0.25$) is reduced. Furthermore, except the u_y at $\theta = 60°$ in Fig. 11b, all the (u_x, u_y, u_z) in Fig. 11 show a very-slightly non-smooth continuation across the interface plane.

Fig. 12 shows the variations of the six stresses $(\sigma_{xx}, \sigma_{xy}, \sigma_{xz}, \sigma_{yy}, \sigma_{yz}, \sigma_{zz})$ along $-5\,\text{m} \le x \le 5\,\text{m}$ at ($y = 0.5$ m and $z = 1$ m) for the dip angle θ value of $30°$, $60°$, $90°$, $120°$, or $150°$. Table 1 presents the stress jumps across the material interface plane. The effects of the bi-materials to the six stress values are evident comparing to these of the two homogeneous elastic halfspaces. In particular, σ_{xx}, σ_{xy} and σ_{xz} are discontinuous across the material interface plane for θ=30°, 60°, 120° or 150°. σ_{yy}, σ_{yz} and σ_{zz} are always discontinuous across the material interface plane for θ=30°, 60°, 90°, 120° or 150°. The corresponding stress jumps are between 0.1489 MPa and 41.1799 MPa. At some interface points, some stresses (such as $\sigma_{xx}, \sigma_{xy}, \sigma_{xz}, \sigma_{yz}, \sigma_{zz}$) can have some very high values comparing to the values at other locations and the results of the homogeneous halfspace models.

Furthermore, the BEM results for the jumps ($\Delta\sigma_{ij} = \left| \sigma_{ij}\left(x = c'^{+} \right) - \sigma_{ij}\left(x = c'^{-} \right) \right|$) of σ_{xx}, σ_{xy} and σ_{xz} values at the interface plane for θ=90° are between 0.0001 MPa and 0.0009 MPa (Table 1) and very close to the theoretical zero (0) value since the three stresses are non-smoothly continuous at the interface plane [8, 9, 25]. Such near zero stresses jumps for θ=90° can indicate that the proposed BEM method is of high accuracy.

7.1.3 Elastic fields on the horizontal plane z = 1 m for $\theta = 60°$

Fig. 13 shows the variations of (u_x, u_y, u_z) on the horizontal plane area $(-5\text{ m} \le x \le 5\text{ m}, \ 0 \le y \le 5\text{ m})$ at $z = 1$ m for $\theta = 60^{\circ}$, respectively. As shown in Fig. 11a, u_x has a slightly non-smooth continuation at the point $(x = c' = 0.5774\text{ m}, \ y = 0.5\text{ m}, \ z = 1\text{ m})$ on the material interface. Fig. 13a further shows that u_x has a slightly non-smooth continuation across the material interface line of $(x = c' = 0.5774\text{ m}, \ 0 \le y \le 5\text{ m}, \ z = 1\text{ m})$. Fig. 13a and 13c show the both u_x and u_z decrease as y increases from 0 to 5 m. u_y is zero along the symmetrical line $y = 0$ and $-5\text{ m} \le x \le 5\text{ m}$. u_y has two peak values and increases at the beginning and then decrease as y increases. The displacement u_y is non-smoothly continuous at the point $(x = c' = 0.5774\text{ m}, \ 0 \le y \le 0.5\text{ m}, \ z = 1\text{ m})$ on the material interface.

Fig. 14 shows the variations of the six stresses $(\sigma_{xx}, \sigma_{xy}, \sigma_{xz}, \sigma_{yy}, \sigma_{yz}, \sigma_{zz})$ over the above horizontal area $(-5\text{ m} \le x \le 5\text{ m}, \ 0 \le y \le 5\text{ m})$ covering the square footing area at $z=1$ m for $\theta = 60^{\circ}$. σ_{xy} and σ_{yz} are zero along the anti-symmetrical line $y = 0$. In this way, other stress components except σ_{xy} and σ_{yz} are discontinuous across the material interface line of $(x = c' = 0.5774\text{ m}, \ 0 \le y \le 5\text{ m}, \ z = 1\text{ m})$. As y increases, the absolute values of σ_{xx}, σ_{xz} and σ_{zz} decrease in general and the absolute values of σ_{xy}, σ_{yy} and σ_{yz} first increase and then decreases.

7.1.4 Elastic fields at different z for y = 0.5 m and θ = 60°

Fig. 15 shows the variations of (u_x, u_y, u_z) with x $(-5\text{ m} \le x \le 5\text{ m})$ with different z values at $y = 0.5$ m and $\theta = 60^{\circ}$. As z increases, (u_x, u_y, u_z) decrease in general. The effect of the inclined bi-material properties is clearly shown in Fig. 15. At the bi-material interface points, u_x and u_y have clear non-smooth continuation properties whilst u_z has less evident non-smooth continuation feature.

Considering the importance of the Mises stress in analyzing the yielding state, Fig. 16 presents the variations of the Mises stress with x $(-5\,\text{m} \le x \le 5\,\text{m})$ with different z values at $y = 0.5$ m and $\theta = 60°$. The Mises stress is defined as

$$\sigma_e = \frac{1}{\sqrt{2}}\left[\left(\sigma_{xx} - \sigma_{yy}\right)^2 + \left(\sigma_{yy} - \sigma_{zz}\right)^2 + \left(\sigma_{zz} - \sigma_{xx}\right)^2 + 6\left(\sigma_{xy}^2 + \sigma_{yz}^2 + \sigma_{zx}^2\right)\right]^{1/2} \tag{20}$$

It can be found that the Mises stress has step discontinuation at the material interface points. As z increases, the absolute values and the discontinuous values of the Mises stress decrease in general. The effect of the bi-materials with inclined interface can be clearly observed in the non-regular variations of the Mises stress with x and z.

7.2. Square footing on three material halfspace with two non-horizontal interfaces

7.2.1 General

The present BEM program is further used to examine the elastic field in a three-material halfspace with two non-horizontal and parallel interfaces subject to the square footing pressure of 100 MPa (Fig. 17). The three materials have the elastic parameters as follows: $(E_1 = 20\,\text{GPa}, v_1 = 0.3)$, $(E_2 = 40\,\text{GPa}, v_2 = 0.25)$ and $(E_3 = 20\,\text{GPa}, v_3 = 0.3)$, respectively. In other words, the materials 1 and 3 have the same elastic properties and the material 2 is their sandwich.

In Fig. 17a, the points a and b are at $x = -1$ m and 1 m on the boundary urface ($z=0$), respectively. In Fig. 17b, c_1' and c_2' are the horizontal distances from the points c_1 and c_2 on the material interfaces to the vertical coordinate plane Oyz along the x-axis direction, respectively. For $\theta = 30°, 60°, 90°, 120°$ and $150°$, the c_1' values are equal to 0.7321, 0.4226, -1, -1.5774 and -2.7321 m, respectively and the c_2' values are equal to 2.7321, 1.5774, 1, 0.4226 and 0.7321 m, respectively. The adopted boundary meshes are similar to those shown in Fig. 9. The discontinuous elements are positioned on the two sides of each of the two material interface strike lines ($x = 1$ m and $z = 0$) and ($x = -1$ m and $z=0$). The adopted boundary meshes have a total of 320 finite elements (248 type I elements and 72 type II

elements) and a total of 64 infinite elements (56 type III elements, 4 type IV elements and 4 type V elements).

7.2.2 Numerical results

Fig. 18 shows the variations of three displacements (u_x, u_y, u_z) with x ($-5\,\text{m} \le x \le 5\,\text{m}$) at $y = 0.5$ m and $z = 1$ m for $\theta = 30°$, $60°$, $90°$, $120°$, or $150°$. The results of two homogeneous elastic halfspaces (i.e., $\theta = 0°$ or $180°$) are also presented in Fig. 18. The two curves of each component of (u_x, u_y, u_z) for $\theta = 30°$ and $\theta = 150°$ (similarly or $\theta = 60°$ and $\theta = 120°$) have the symmetrical or anti-symmetrical variations with respect to the x axis, which is consistent to the fact that the materials 1 and 3 have the same elastic properties and each pair of the elastostatic problems are symmetrically identical. The effects of the three materials with inclined two interface planes to the elastic displacements are evidently shown with respect to the results of the two homogeneous halfspaces. The results of the two homogeneous halfspaces can offer the upper or lower bounds for the results of the three-material halfspace models.

Fig. 19 shows the variations of $(\sigma_{xx}, \sigma_{xy}, \sigma_{xz}, \sigma_{yy}, \sigma_{yz}, \sigma_{zz})$ with $x (-5\,\text{m} \le x \le 5\,\text{m})$ with different θ values at $y = 0.5$ m and $z = 1$ m. Table 1 also presents the stress jumps ($\Delta\sigma_{ij} = \left| \sigma_{ij}\left(x = c_1'^{+} \text{ or } c_2'^{+}\right) - \sigma_{ij}\left(x = c_1'^{-} \text{ or } c_2'^{-}\right) \right|$) in three-material halfspace for different z across the material interface plane. Similarly the symmetrical and/or anti-symmetrical results are obtained for the six stresses for each pair of the three-material halfspace problem. The effects of the three materials with two inclined interface planes to the elastic stresses are evidently shown with respect to the results of the two homogeneous halfspaces. At each interface point, some stresses (such as $\sigma_{xx}, \sigma_{yy}, \sigma_{yz}$) can have some very high values comparing to the values at other locations and the results of the homogeneous halfspace models.

7.3 Further analysis of displacements and stresses across material interfaces

The elastic fields in a bi-material or three-material halfspace with non-horizontally oriented interface planes due to tractions are presented and examined in detail. The effects of the

inclined material interface to the elastic displacements and stresses are analyzed with respect to the results of homogeneous elastic halfspace. Across the material interface, the elastic displacements are non-smoothly continuous to different degrees, which is affected by the interface declination angle θ. Across the material interfaces, all the six stress components can have step-discontinuation for $\theta \neq 90^o$ whereas only the three stresses σ_{yy}, σ_{yz} and σ_{zz} are step-discontinuous for $\theta=90^o$. Distribution of the stresses in a non-horizontally layered halfspace is different to those in a homogeneous halfspace due to the same loading. In particular, some stress components can have very high values at and adjacent the interface planes, which can be important to tensile or shear failures in non-homogeneous materials.

8. Summary and conclusions

<mark>This paper adopts</mark> the generalized Kelvin solution of a multilayered solid and develops a new BEM program for the effect and efficient analysis and calculation of the elastic field in non-horizontally layered halfspace subject to tractions. The BEM program uses five boundary element techniques to handle the mixtures of the boundary surface conditions. They include the material interface strike line and the infinite extension of both boundary surface areas and the strike lines.

The use of the generalized Kelvin solution can eliminate the requirement of mesh discretization for the internal material interface planes. The only surface that needs to be discretized is the horizontal boundary surface of infinite extent. The infinite boundary elements are used to effectively and efficiently take into account the influence of a far region to the numerical approach. The finite and infinite discontinuous boundary elements are introduced to overcome the numerical problems due to the step-discontinuous material property across the interface strikes on the boundary surface. Consequently, the singular integrals in the governing boundary integral equations are calculated using the existing numerical integration techniques. Numerical results for some typical elastostatic problems presented in the paper indicate that the BEM program can be used for the elastic fields in the non-horizontal layered halfspace.

More detailed investigations need to be carried for accurately enhance our knowledge and

capability for the related problems in science and engineering in the future. The numerical results presented in this paper are due to the completely flexible footing loading. The BEM program can be applied to examine the contact problems where the rigid or elastic footing can be used because of the adoption of the discontinuous elements.

Acknowledgements

Appendix A. The kernel functions U_{ijk}^Y and T_{ijk}^Y

The kernel functions U_{ijk}^Y and T_{ijk}^Y in Eq. (3) can be described by using the constitutive equations as follows

$$U_{ijk}^Y = \lambda \delta_{ij} U_{mmk}^\varepsilon + 2\mu U_{ijk}^\varepsilon \tag{A.1}$$

$$T_{ijk}^Y = \lambda \delta_{ij} T_{mmk}^\varepsilon + 2\mu T_{ijk}^\varepsilon \tag{A.2}$$

where λ and μ are Lamé constants, and U_{ijk}^ε and T_{ijk}^ε can be written as

$$U_{ijk}^\varepsilon = \left(u_{ik,j}^Y + u_{jk,i}^Y \right)/2 \tag{A.3}$$

$$T_{ijk}^\varepsilon = \left(t_{ik,j}^Y + t_{jk,i}^Y \right)/2 \tag{A.4}$$

The derivatives of the displacements in Eq. (A.3) are approximated as

$$\frac{\partial u_{ik}^Y}{\partial x} \approx \frac{1}{2D} \left[u_{ik}^Y \left(x+D, y, z \right) - u_{ik}^Y \left(x-D, y, z \right) \right] \tag{A.5}$$

$$\frac{\partial u_{ik}^Y}{\partial y} \approx \frac{1}{2D} \left[u_{ik}^Y \left(x, y+D, z \right) - u_{ik}^Y \left(x, y-D, z \right) \right] \tag{A.6}$$

$$\frac{\partial u_{ik}^Y}{\partial z} \approx \frac{1}{2D} \left[u_{ik}^Y \left(x, y, z+D \right) - u_{ik}^Y \left(x, y, z-D \right) \right] \tag{A.7}$$

where x, y, z are the coordinates of the source point p in the global coordinate system $Oxyz$ and D is the distance between the two source points. The derivatives of the tractions in Eq. (A.4) can also be calculated using the above methods.

In order to calculate the derivatives $u_{ik,j}^Y$ and $t_{ik,j}^Y$, it is necessary to compute the displacements and stresses of the fundamental solution at six points in the neighborhood of the source point p. The choice of the interval D is a crucial decision and an extensive numerical investigation is executed in Pan and Yuan [35] and Tonon $et\ al.$ [38]. The best D value is $10^{-6} r$ where r is the distance between the source and field points.

Appendix B. The fundamental solution in $O'x'y'z'$ coordinates

For a layered medium, shown in Fig. 3, the vector fields of displacements, vertical stresses and plane strains are defined as

$$\boldsymbol{u} = \begin{bmatrix} u_{x'} & u_{y'} & u_{z'} \end{bmatrix}^{\mathrm{T}}, \quad \boldsymbol{T}_{z'} = \begin{bmatrix} \sigma_{x'z'} & \sigma_{y'z'} & \sigma_{z'z'} \end{bmatrix}^{\mathrm{T}}, \quad \boldsymbol{\Gamma}_p = \begin{bmatrix} \varepsilon_{x'x'} & \varepsilon_{x'y'} & \varepsilon_{y'y'} \end{bmatrix}^{\mathrm{T}} \tag{B.1}$$

where the superscript T stands for the transpose of a matrix.

For concentrated point loads, i.e., $\boldsymbol{F}_c = \begin{bmatrix} f_{x'} & f_{y'} & f_{z'} \end{bmatrix}^{\mathrm{T}}$, the solution expressions of the layer medium are presented as follows

$$\boldsymbol{u} = \boldsymbol{G}_u \boldsymbol{F}_c, \quad \boldsymbol{T}_z = \boldsymbol{G}_z \boldsymbol{F}_c, \quad \boldsymbol{\Gamma}_z = \boldsymbol{G}_p \boldsymbol{F}_c. \tag{B.2}$$

where the matrices $\boldsymbol{G}_u$, $\boldsymbol{G}_z$ and $\boldsymbol{G}_p$ can be expressed as

$$2\pi \boldsymbol{G}_u \left(x', y', z' \right) = \int_0^\infty \begin{pmatrix} \Phi_1 J_0 - \dfrac{x'^2 - y'^2}{r^2} \Phi_2 J_2 & -\dfrac{2x'y'}{r^2} \Phi_2 J_2 & -\dfrac{x'}{r} \Phi_{13} J_1 \\[2ex] -\dfrac{2x'y'}{r^2} \Phi_2 J_2 & \Phi_1 J_0 + \dfrac{x'^2 - y'^2}{r^2} \Phi_2 J_2 & -\dfrac{y'}{r} \Phi_{13} J_1 \\[2ex] \dfrac{x'}{r} \Phi_{31} J_1 & \dfrac{y'}{r} \Phi_{31} J_1 & \Phi_{33} J_0 \end{pmatrix} d\rho \tag{B.3}$$

$$2\pi \boldsymbol{G}_z \left(x', y', z' \right) = \int_0^\infty \begin{pmatrix} \Psi_1 J_0 - \dfrac{x'^2 - y'^2}{r^2} \Psi_2 J_2 & -\dfrac{2x'y'}{r^2} \Psi_2 J_2 & -\dfrac{x'}{r} \Psi_{13} J_1 \\[2ex] -\dfrac{2x'y'}{r^2} \Psi_2 J_2 & \Psi_1 J_0 + \dfrac{x'^2 - y'^2}{r^2} \Psi_2 J_2 & -\dfrac{y'}{r} \Psi_{13} J_1 \\[2ex] \dfrac{x'}{r} \Psi_{31} J_1 & \dfrac{y'}{r} \Psi_{31} J_1 & \Psi_{33} J_0 \end{pmatrix} \rho d\rho \tag{B.4}$$

$$2\pi \boldsymbol{G}_p\left(x', y', z'\right) = -\frac{1}{2}\int_0^\infty \begin{pmatrix} \dfrac{x'}{r}\left(2\Phi_1+\Phi_2\right)J_1 & \dfrac{y'}{r}\Phi_2 J_1 & \Phi_{13}J_0 \\[2mm] \dfrac{y'}{r}\Phi_1 J_1 & \dfrac{x'}{r}\Phi_1 J_1 & 0 \\[2mm] \dfrac{x'}{r}\Phi_2 J_1 & \dfrac{y'}{r}\left(2\Phi_1+\Phi_2\right)J_1 & \Phi_{13}J_0 \end{pmatrix}\rho\,d\rho$$

$$+\frac{1}{2}\int_0^\infty \begin{pmatrix} \left(\dfrac{4x'^3}{r^3}-\dfrac{3x'}{r}\right)\Phi_2 J_3 & \left(\dfrac{3y'}{r}-\dfrac{4y'^3}{r^3}\right)\Phi_2 J_3 & \dfrac{x'^2-y'^2}{r^2}\Phi_{13}J_2 \\[2mm] \left(\dfrac{3y'}{r}-\dfrac{4y'^3}{r^3}\right)\Phi_2 J_3 & \left(\dfrac{3x'}{r}-\dfrac{4x'^3}{r^3}\right)\Phi_2 J_3 & \dfrac{2x'y'}{r^2}\Phi_{13}J_2 \\[2mm] \left(\dfrac{3x'}{r}-\dfrac{4x'^3}{r^3}\right)\Phi_2 J_3 & \left(\dfrac{4y'^3}{r^3}-\dfrac{3y'}{r}\right)\Phi_2 J_3 & \dfrac{y'^2-x'^2}{r^2}\Phi_{13}J_2 \end{pmatrix}\rho\,d\rho$$

(B.5)

where $r=\sqrt{x'^2+y'^2}$, $\Phi_1=\tfrac{1}{2}\left[\Phi_{11}+\Phi_{22}\right]$, $\Phi_2=\tfrac{1}{2}\left[\Phi_{11}-\Phi_{22}\right]$, $\Psi_1=\tfrac{1}{2}\left[\Psi_{11}+\Psi_{22}\right]$ and

$\Psi_2=\tfrac{1}{2}\left[\Psi_{11}-\Psi_{22}\right]$. The following identity of Bessel functions (J_m) of order m is used in the further reduction

$$\frac{1}{2\pi}\int_0^{2\pi} e^{\pm i\left(\rho r\sin\psi-m\psi\right)}d\psi = J_m\left(\rho r\right)=J_m,\quad m=0,\pm1,\pm2,\cdots. \tag{B.6}$$

The expressions of the matrices $\boldsymbol{G}_u$, $\boldsymbol{G}_z$ and $\boldsymbol{G}_p$ include the inverse Hankel transform integrals with a semi-infinite interval. The expressions also include the Bessel functions of order of zero, unit and second and ten fundamental functions of Φ_{11}, Φ_{13}, Φ_{22}, Φ_{31}, Φ_{33}, Ψ_{11}, Ψ_{13}, Ψ_{22}, Ψ_{31}, and Ψ_{33}. A proceeding limit technique, based on an adaptively iterative Simpson's quadrature, is adopted in the evaluation of the inverse Hankel transform integrals in Eqs. (B.3) to (B.5). Using the procedure, the semi-infinite interval of the inverse Hankel transform integrals can be accommodated and the improper integrals can be efficiently evaluated with high and controlled accuracy.

The solutions of the plane stresses $\left(\sigma_{x'x'},\sigma_{x'y'},\sigma_{y'y'}\right)$ and the vertical strains $\left(\varepsilon_{x'z'},\varepsilon_{y'z'},\varepsilon_{z'z'}\right)$ due to the point loads $\left(f_{x'},f_{y'},f_{z'}\right)$ can be easily obtained from the solutions of the vertical stresses $\left(\sigma_{x'z'},\sigma_{y'z'},\sigma_{z'z'}\right)$ and the plane strains $\left(\varepsilon_{x'x'},\varepsilon_{x'y'},\varepsilon_{y'y'}\right)$ by using the constitutive equations.

More details of the expressions and mathematical properties of the fundamental solution can be found in Yue [12].

Appendix C. The fundamental solution in $Oxyz$ coordinates

C.1. The solution in $O'x'y'z'$ coordinates due to f_x

The point force f_x in $Oxyz$ can be re-expressed as follows in the coordinate system $O'x'y'z'$,

$$f_{x'} = f_x \cos\theta, \quad f_{y'} = 0, \quad f_{z'} = -f_x \sin\theta \tag{C.1}$$

The displacements and stresses in the system $O'x'y'z'$ induced by $f_x = 1$ can be calculated using the equations

$$u_{i'} = u_{i'}\big|_{f_{x'}=1} \cos\theta - u_{i'}\big|_{f_{z'}=1} \sin\theta \tag{C.2}$$

$$\sigma_{i'j'} = \sigma_{i'j'}\big|_{f_{x'}=1} \cos\theta - \sigma_{i'j'}\big|_{f_{z'}=1} \sin\theta \tag{C.3}$$

where $u_{i'}\big|_{f_{x'}=1}$ and $\sigma_{i'j'}\big|_{f_{x'}=1}$ are the displacements and stresses induced by $f_{x'} = 1$, and $u_{i'}\big|_{f_{z'}=1}$ and $\sigma_{i'j'}\big|_{f_{z'}=1}$ are the displacements and stresses induced by $f_{z'} = 1$, respectively.

C.2. The solution in $O'x'y'z'$ coordinates due to f_y

The point force f_y in $Oxyz$ can be re-expressed as follows in the coordinate system $O'x'y'z'$,

$$f_{x'} = 0, \quad f_{y'} = f_y, \quad f_{z'} = 0 \tag{C.4}$$

The displacements and stresses in the $O'x'y'z'$ system induced by $f_y = 1$ can be calculated using the equations

$$u_{i'} = u_{i'}\big|_{f_{y'}=1} \tag{C.5}$$

$$\sigma_{i'j'} = \sigma_{i'j'}\big|_{f_{y'}=1} \tag{C.6}$$

where $u_{i'}\big|_{f_{y'}=1}$ and $\sigma_{i'j'}\big|_{f_{y'}=1}$ are the displacements and stresses induced by $f_{y'} = 1$.

C.3. The solution in $O'x'y'z'$ coordinates due to f_z

The point force f_z in *Oxyz* can be re-expressed as follows in the coordinate system $O'x'y'z'$,

$$f_{x'} = f_z \sin\theta, \quad f_{y'} = 0, \quad f_{z'} = f_z \cos\theta \tag{C.7}$$

The displacements and stresses in the system $O'x'y'z'$ induced by $f_z = 1$ can be calculated using the equations

$$u_{i'} = u_{i'}\big|_{f_{x'}=1} \sin\theta + u_{i'}\big|_{f_{z'}=1} \cos\theta \tag{C.8}$$

$$\sigma_{i'j'} = \sigma_{i'j'}\big|_{f_{x'}=1} \sin\theta + \sigma_{i'j'}\big|_{f_{z'}=1} \cos\theta \tag{C.9}$$

where $u_{i'}\big|_{f_{x'}=1}$, $\sigma_{i'j'}\big|_{f_{x'}=1}$, $u_{i'}\big|_{f_{z'}=1}$ and $\sigma_{i'j'}\big|_{f_{z'}=1}$ have the same meanings as defined in Eqs. (C.2) and (C.3).

C.4. The solutions in Oxyz coordinates

The generalized Kelvin solution (u_i and σ_{ij}) in *Oxyz* coordinates induced by the point body force vector (f_x, f_y, f_z) have the following matrix transformation relationship with the generalized Kelvin in $O'x'y'z'$ coordinates induced by the point body force vector $(f_{x'}, f_{y'}, f_{z'})$

$$u_i = \beta_{ii'} u_{i'} \quad (i = x, y, z, i' = x', y', z') \tag{C.10}$$

$$\sigma_{ij} = \beta_{ii'} \beta_{jj'} \sigma_{i'j'} \quad (i, j = x, y, z, i', j' = x', y', z') \tag{C.11}$$

where $\beta_{ii'}$ are the coefficients of the coordinate transform matrix.

The coordinates at any point in the coordinate system $O'x'y'z'$ can be obtained from the ones in the coordinate system *Oxyz* by

$$x' = \beta_{x'x}(x - d_1) + \beta_{x'y}y + \beta_{x'z}z \tag{C.12}$$

$$y' = \beta_{y'x}(x - d_1) + \beta_{y'y}y + \beta_{z'z}z \tag{C.13}$$

$$z' = \beta_{z'x}(x - d_1) + \beta_{z'y}y + \beta_{z'z}z \tag{C.14}$$

where d_1 is the distance between the two origins O and O', and $\beta_{i'i}$ are the coefficients of the coordinate transform.

Appendix D. The interpolation functions for five element types

D.1. Shape functions for continuous finite boundary element (type I)

$$N_1 = -0.25(1-\xi)(1-\eta)(1+\xi+\eta)$$

$$N_2 = -0.25(1+\xi)(1-\eta)(1-\xi+\eta)$$

$$N_3 = -0.25(1+\xi)(1+\eta)(1-\xi-\eta)$$

$$N_4 = -0.25(1-\xi)(1+\eta)(1+\xi-\eta)$$

$$N_5 = 0.5(1-\xi^2)(1-\eta)$$

$$N_6 = 0.5(1-\eta^2)(1+\xi)$$

$$N_7 = 0.5(1-\xi^2)(1+\eta)$$

$$N_8 = 0.5(1-\eta^2)(1-\xi) \tag{D.1}$$

D.2. Shape functions for discontinuous finite boundary element (type II)

$$N_1 = -0.3(1-\xi)(1-\eta)(1+\xi+1.5\eta)$$

$$N_2 = -0.3(1+\xi)(1-\eta)(1-\xi+1.5\eta)$$

$$N_3 = -0.3(1+\xi)(2/3+\eta)(1-\xi-\eta)$$

$$N_4 = -0.3(1-\xi)(2/3+\eta)(1+\xi-\eta)$$

$$N_5 = 0.6(1-\xi^2)(1-\eta)$$

$$N_6 = 0.75(1+\xi)(1-\eta)(2/3+\eta)$$

$$N_7 = 0.6(1-\xi^2)(2/3+\eta)$$

$$N_8 = 0.75(1-\xi)(1-\eta)(2/3+\eta) \tag{D.2}$$

D.3. Interpolation functions for continuous infinite elements (type III)

D.3.1. Shape functions

$$^{\infty}N_1 = \xi\eta(1-\xi)/(1-\eta)$$

$$^{\infty}N_2 = -\xi\eta(1+\xi)/(1-\eta)$$

$$^{\infty}N_3 = 0.5\xi(1+\xi)(1+\eta)/(1-\eta)$$

$$^{\infty}N_4 = 0.5\xi(\xi-1)(1+\eta)/(1-\eta)$$

$$^{\infty}N_5 = -2\eta(1-\xi^2)/(1-\eta)$$

$$^{\infty}N_6 = (1-\xi^2)(1+\eta)/(1-\eta) \tag{D.3}$$

D.3.2. Interpolation functions of displacements

$$^{\infty}N_1^u = 0.25\xi(\xi-1)(1-\eta)$$

$$^{\infty}N_2^u = 0.25\xi(\xi+1)(1-\eta)$$

$$^{\infty}N_5^u = 0.5(1-\xi^2)(1-\eta) \tag{D.4}$$

D.3.3. Interpolation functions of tractions

$$^{\infty}N_1^t = 0.125\xi(\xi-1)(1-\eta)^2$$

$$^{\infty}N_2^t = 0.125\xi(\xi+1)(1-\eta)^2$$

$$^{\infty}N_5^t = 0.25(1-\xi^2)(1-\eta)^2 \tag{D.5}$$

D.4. Interpolation functions for discontinuous infinite elements (type IV)

D.4.1. Shape functions

$$^{\infty}N_1 = -1.8\xi\eta(\xi-1)/(1-\eta)$$

$$^{\infty}N_2 = -1.2\xi\eta(\xi+2/3)/(1-\eta)$$

$$^{\infty}N_3 = 0.6\xi(\xi+2/3)(1+\eta)/(1-\eta)$$

$$^{\infty}N_4 = 0.9\xi(\xi-1)(1+\eta)/(1-\eta)$$

$$^{\infty}N_5 = -3\eta(1-\xi)(2/3+\xi)/(1-\eta)$$

$$^{\infty}N_6 = 1.5(1-\xi)(2/3+\xi)(1+\eta)/(1-\eta) \tag{D.6}$$

D.4.2. Interpolation functions of displacements

$$^{\infty}N_1^u = 0.45(1-\eta)\xi(\xi-1)$$

$$^{\infty}N_2^u = 0.3(1-\eta)\xi(\xi+2/3)$$

$$^{\infty}N_5^u = 0.75(1-\eta)(1-\xi)(\xi+2/3) \tag{D.7}$$

D.4.3. Interpolation functions of tractions

$$^{\infty}N_1^t = 0.225(1-\eta)^2\xi(\xi-1)$$

$$^{\infty}N_2^t = 0.15(1-\eta)^2\xi(2/3+\xi)$$

$$^{\infty}N_5^t = 0.375(1-\eta)^2(1-\xi)(2/3+\xi) \tag{D.8}$$

D.5. Interpolation functions for discontinuous infinite elements (type V)

D.5.1. Shape functions

$$^{\infty}N_1 = -1.2\eta(\xi-2/3)/(1-\eta)$$

$$^{\infty}N_2 = -1.8\xi\eta(\xi+1)/(1-\eta)$$

$$^{\infty}N_3 = 0.9\xi(\xi+1)(1+\eta)/(1-\eta)$$

$$^{\infty}N_4 = 0.6\xi(\xi-2/3)(1+\eta)/(1-\eta)$$

$$^{\infty}N_5 = -3\eta(2/3-\xi)(1+\xi)/(1-\eta)$$

$$^{\infty}N_6 = 1.5(2/3-\xi)(1+\xi)(1+\eta)/(1-\eta) \tag{D.9}$$

D.5.2. Interpolation functions of displacements

$$^{\infty}N_1^u = 0.3(1-\eta)\xi(\xi-2/3)$$

$$^{\infty}N_2^u = 0.45(1-\eta)\xi(\xi+1)$$

$$^{\infty}N_5^u = 0.75(1-\eta)(2/3-\xi)(1+\xi) \tag{D.10}$$

D.5.3. Interpolation functions of tractions

$$^{\infty}N_1^t = 0.15(1-\eta)^2\xi(\xi-2/3)$$

$$^{\infty}N_2^t = 0.225(1-\eta)^2\,\xi\,(\xi+1)$$

$$^{\infty}N_5^t = 0.375(1-\eta)^2\,(2/3-\xi)(1+\xi) \tag{D.11}$$

References

[1] Holl DL. Stress transmission in earths. Proceedings of Highway Research Board 1940; 20:709-721.

[2] Burminster DM. The general theory of stresses and displacements in layered systems. I. J Applied Physics 1945; 16:89-93.

[3] Burminster DM. The general theory of stresses and displacements in layered soil systems. II. J Applied Physics 1945; 16:126-127.

[4] Burminster DM. The general theory of stresses and displacements in layered soil systems. III. J Applied Physics 1945; 16:296-302.

[5] King RB. Elastic analysis of some punch problems for a layered medium. Int J Solids Struct 1987; 23:1657-1664.

[6] Sing SJ. Static deformation of a multilayered half-space by internal sources. J Geophys Res 1970; 75:3257-3263.

[7] Pan E. Static response of a transversely isotropic and layered half-space to general dislocation source. Phys Erath Planet Inter 1989; 58:103-117.

[8] Yue ZQ. Yue's solution of classical elasticity in n-layered solids: Part 1, mathematical formulation. Front Struct Civ Eng 2015; 9:215-249.

[9] Yue ZQ. Yue's solution of classical elasticity in n-layered solids: Part 2, mathematical verification. Front Struct Civ Eng 2015; 9:250-285.

[10] Pereira OJB Almeida, Parreira P. Direct evaluation of Cauchy-principal-value integrals in boundary elements for infinite and semi-infinite three-dimensional domains. Eng Anal Bound Elem 1994; 13:313-320.

[11] Moser W, Duenser Ch, Beer G. Mapped infinite elements for 3D multi-region boundary element analysis. Int J Numer Meth Eng 2004; 61:317-328.

[12] Yue ZQ. On generalized Kelvin solutions in a multilayered elastic medium. J Elasticity 1995; 40:1-43.

[13] Watson JO. Advanced implementation of the boundary element method for two- and three-dimensional elastostatics, in Banerjee PK and Butterfield R (eds.), Developments in Boundary Element Methods I, Applied Science, London. 1979, pp. 31-63.

[14] Beer G, Waston JQ, Swoboda G. Three-dimensional analysis of tunnels using infinite boundary elements. Computers Geotech 1987; 3:37-58.

[15] Beer G, Watson JO. Infinite boundary elements. Int J Numer Meth Eng 1989; 28:1233-1247.

[16] Zhang CH, Song CM, Pekau OA. Infinite boundary elements for dynamic problems of 3-D half space. Int J Numer Meth Eng 1991; 31:447-462.

[17] Liu M, Farris TN. Three-dimensional infinite boundary elements for contact problems. Int J Numer Meth Eng 1993; 36: 3381-3398.

[18] Davies TG, Bu S. Infinite boundary elements for the analysis of halfspace problems. Computers Geotech 1996; 19:137-151.

[19] Bu S. Infinite boundary elements for dynamics analysis of machine foundations. Int J Numer Meth Eng, 1997, 40:3901-3917.

[20] Gao XG, Davies TG. 3D infinite boundary elements for half-space problems. Eng Anal Bound Elem 1998; 21:207-213.

[21] Salvadori A. Infinite boundary elements in 2D elasticity. Eng Anal Bound Elem 2008; 32:122-138.

[22] Liang J, Liew KM. Boundary element for half-space problems via fundamental solutions: a three-dimensional analysis. Int J Numer Meth Eng 2001; 52:1189-1202.

[23] Ribeiro DB, Paiva JBD. A new infinite boundary element formulation combined to an alternative multi-region technique. Eng Anal Bound Elem 2013; 37:818-824.

[24] Pan E, Amadei A. Boundary element analysis of fracture mechanics in anisotropic bimaterial. Eng Anal Bound Elem 1999; 23:683-691.

[25] Yue ZQ. On elastostatics of multilayered solids subjected to general surface traction. Quart J Mech Appl Math 1996; 49:471-499.

[26] Merkel R, Kirchgeßner N, Cesa CM, Hoffmann B. Cell force microscopy on elastic layers of finite thickness. Biophysical Journal 2007; 93:3314-3323.

[27] Maloney JM, Walton EB, Bruce CM, Van Vliet KJ. Influence of finite thickness and stiffness on cellular adhesion-induced deformation of compliant substrata. Physical Review E 2008; 78(4):1-15.

[28] Xiao HT, Yue ZQ. Fracture mechanics in layered and graded materials: analysis using boundary element methods. Berlin: De Gruyter and Beijing: Higher Education Press; 2014.

[29] Lachat JC, Waston JO. Effective treatment of boundary integral equations: a formulation for three-dimensional elastostatics. Int J Numer Meth Eng 1976; 10:991-1005.

[30] Beer G, Smith I, Duenser C. The boundary element method with programming for engineering and scientists. New York: Springer Wien; 2008.

[31] Gao XG, Davies TG. Boundary element programming in mechanics. Cambridge: Cambridge University Press; 2002.

[32] Guiggiani M, Gigante A. A general algorithm for multidimensional Cauchy principal value integrals in the boundary element method. ASME J Applied Mechanics 1990; 57: 906-915.

[33] Gao XW. An effective method for numerical evaluation of general 2D and 3D high order singular boundary integrals. Comput Methods Appl Mech Eng 2010; 199: 2856-2864.

[34] Gao XW, Feng WZ, Yang K, Cui M. Projection plane method for evaluation of arbitrary high order singular boundary integrals. Eng Anal Bound Elem 2015; 50:265-274.

[35] Pan E, Yuan FG. Boundary element analysis of three-dimensional crack in anisotropic solids. Int J Numer Meth Eng 2000; 48:211-237.

[36] Kutt HR. Quadrature formulae for finite-part integrals. Special Report WISK 178, National Research Institute for Mathematical Sciences, Pretoria, 1975.

[37] Kutt HR. On the numerical evaluation of finite-part integrals involving an algebraic singularity. Special Report WISK 179, National Research Institute for Mathematical Sciences, Pretoria, 1975.

[38] Tonon F, Pan E, Amadei B. Green's functions and boundary element method formulation for 3D anisotropic media. Computers Struct 2001; 79:469-482.
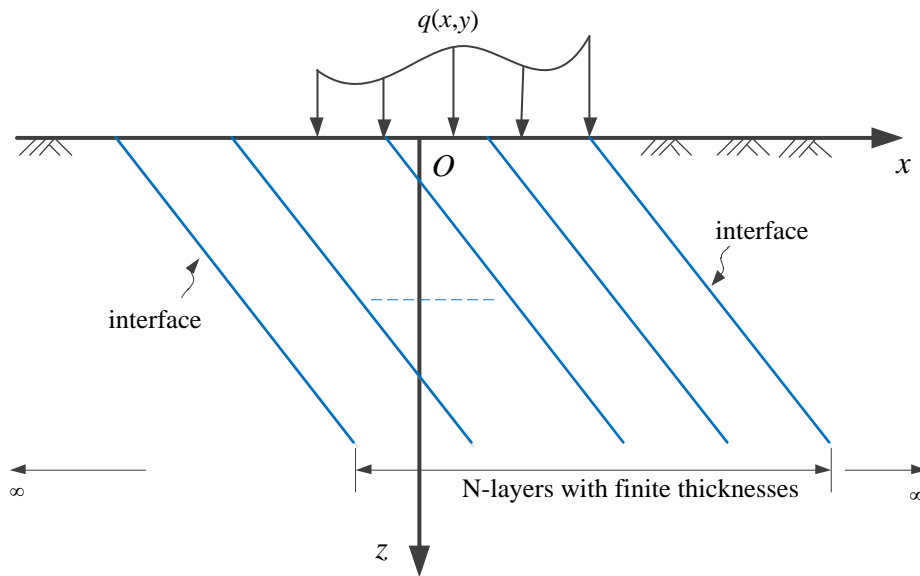
Fig. 1. A layered halfspace subject to distributed loadings on the boundary surface
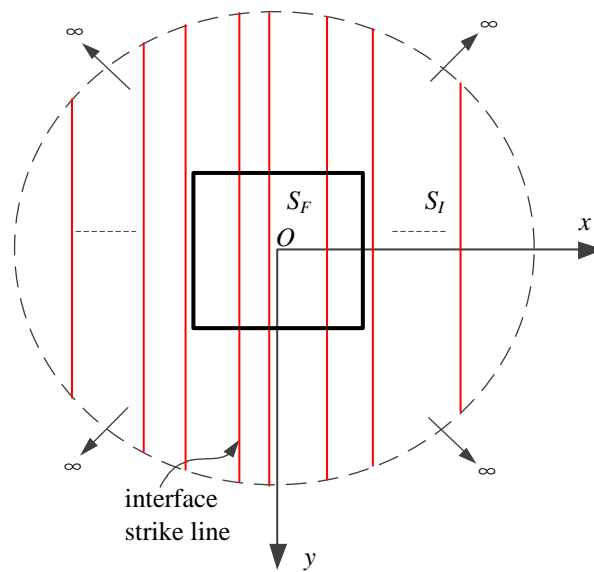
Fig. 2. Definition of S_F and S_I on the boundary surface of a non-horizontally layered halfspace
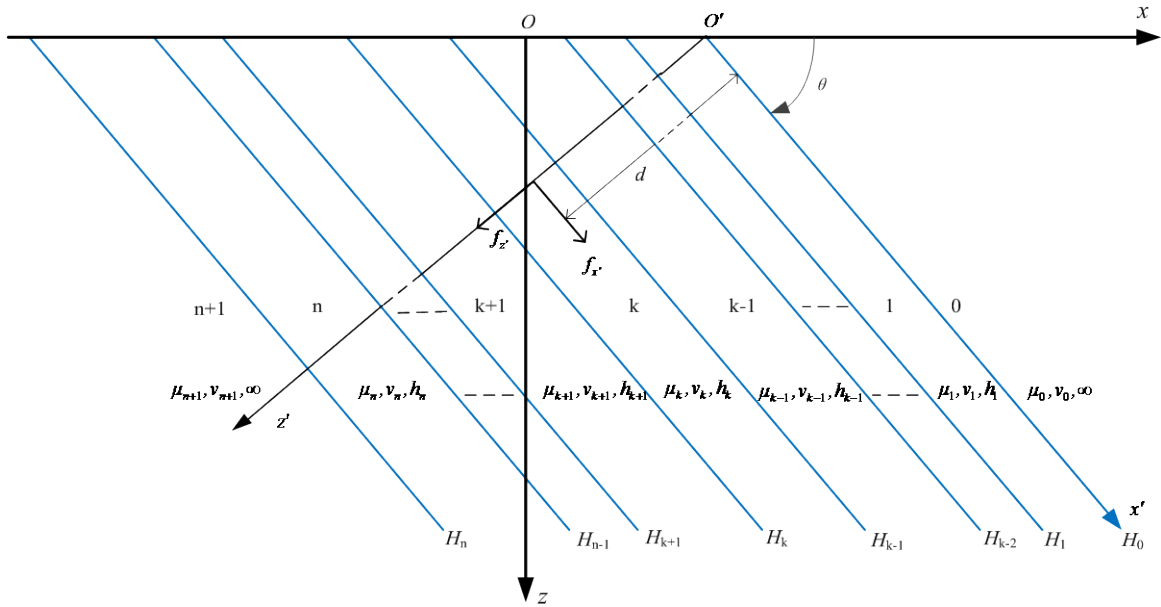
Fig. 3. A multilayered elastic solid of infinite extent subjected to the body forces $f_{x'}$, $f_{y'}$ and $f_{z'}$ concentrated at a point $(0, 0, d)$
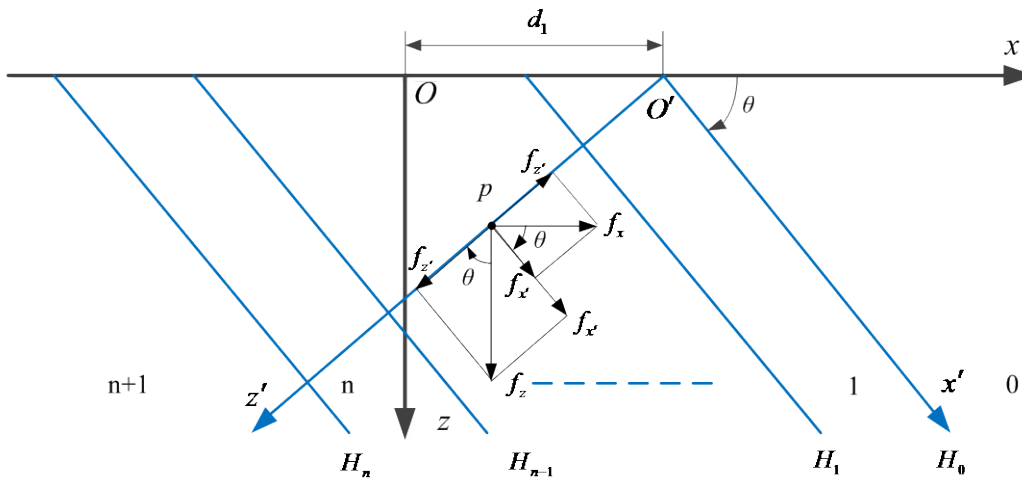
Fig. 4. Relation between two coordinate systems

(a)

(5a) continuous element (type I)

(b)

2/3

interface strike line
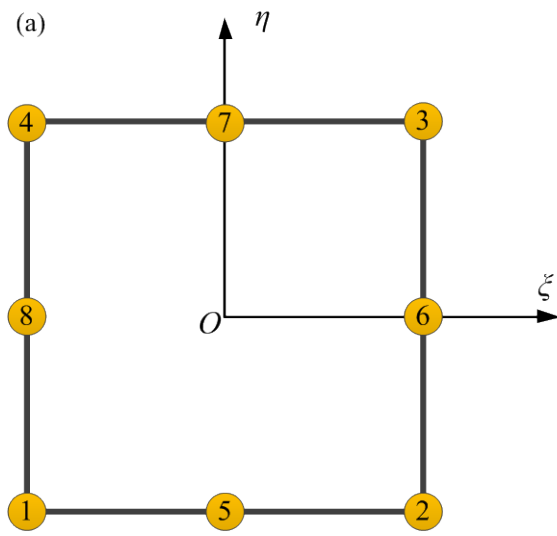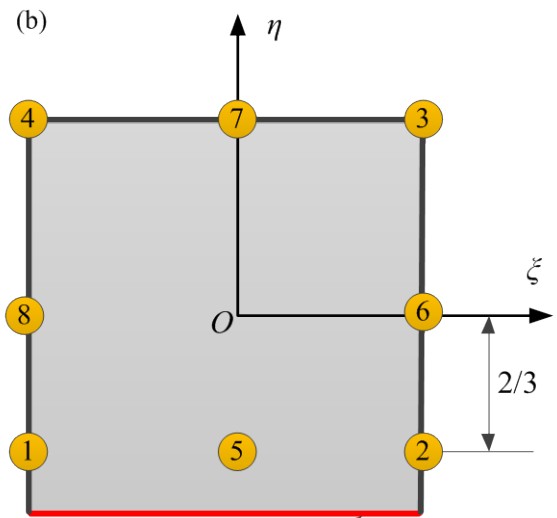
(5b) discontinuous element (type II)

Fig. 5. Two types of finite boundary elements
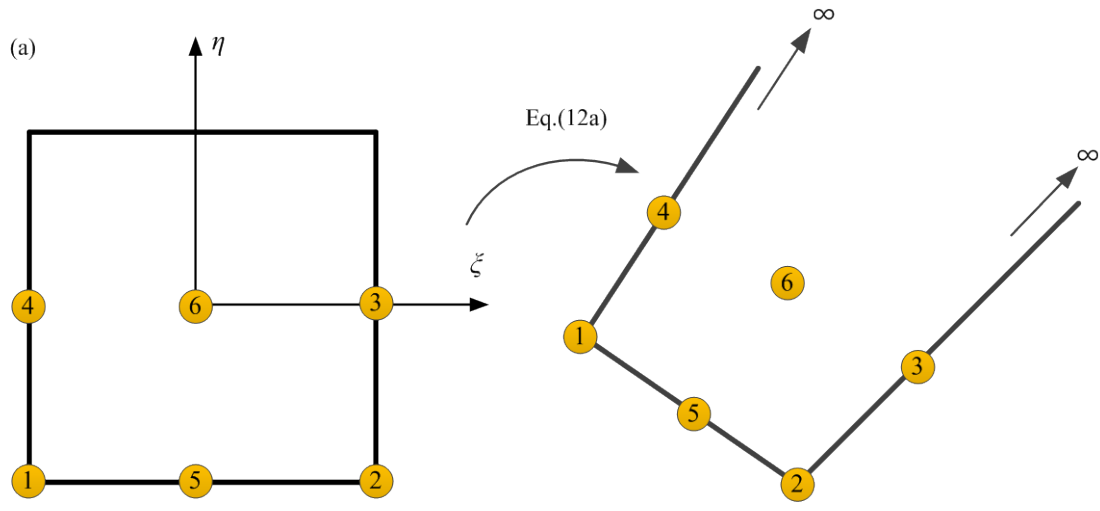
(6a) continuous element (type III)
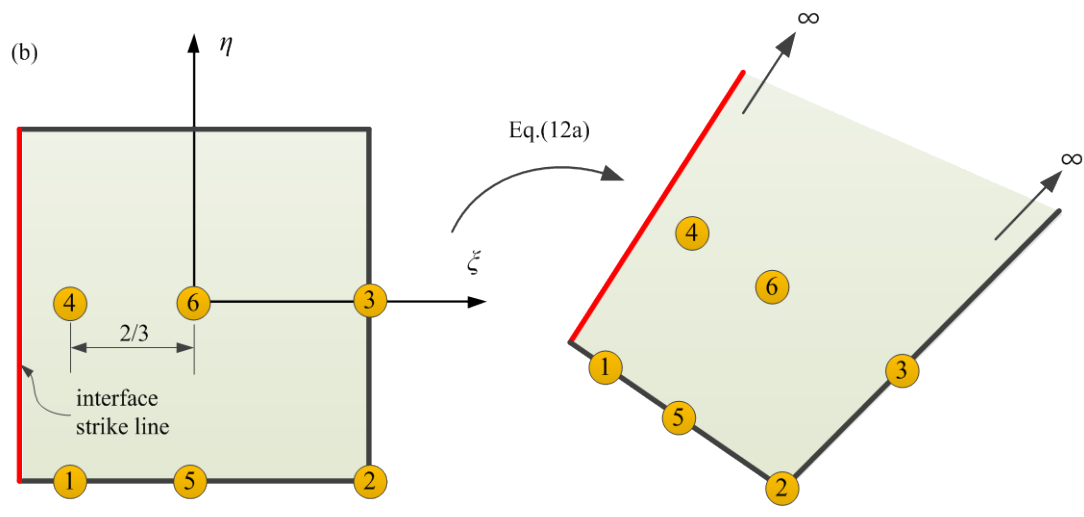
(6b) discontinuous element (type IV)
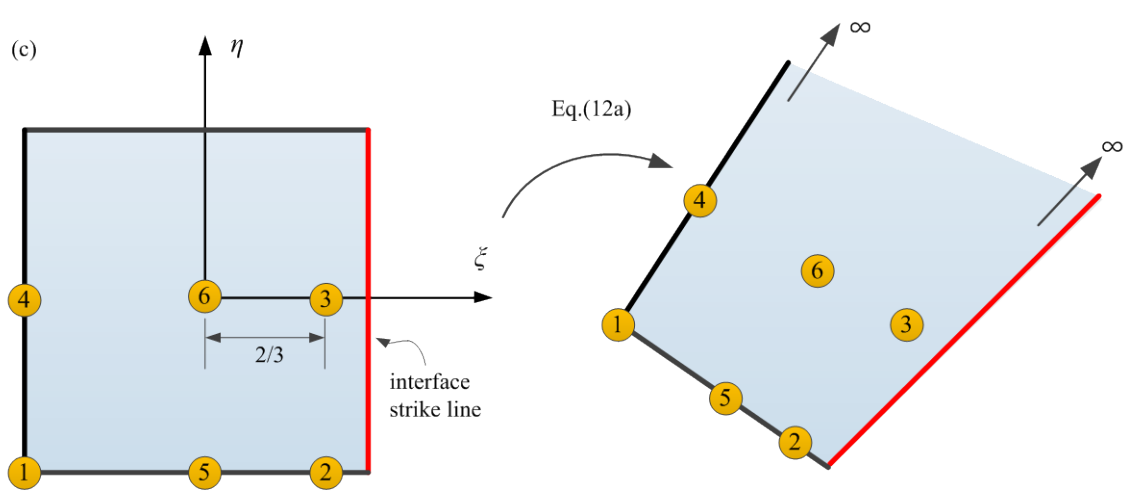
(6c) discontinuous element (type V)

Fig. 6. Three types of infinite boundary elements

(a)

(7a) node 1

(b)

(7b) node 2

(c)
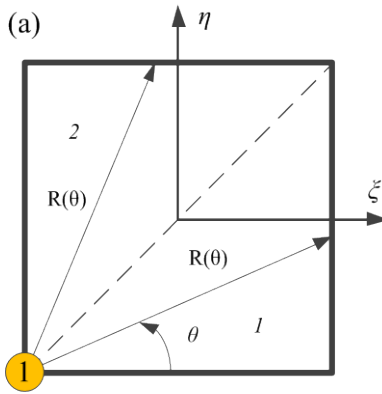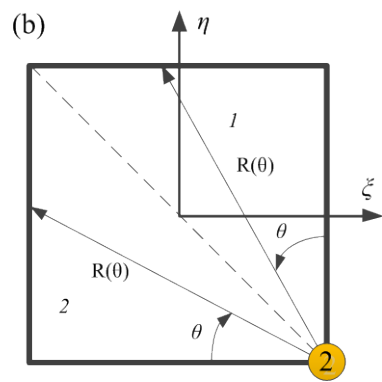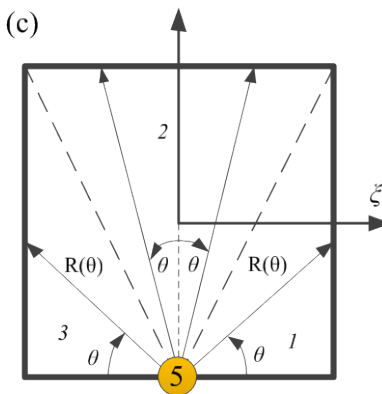
(7c) node 5

Fig. 7. The triangle domain divided in a continuous infinite element (type IV) for different nodes
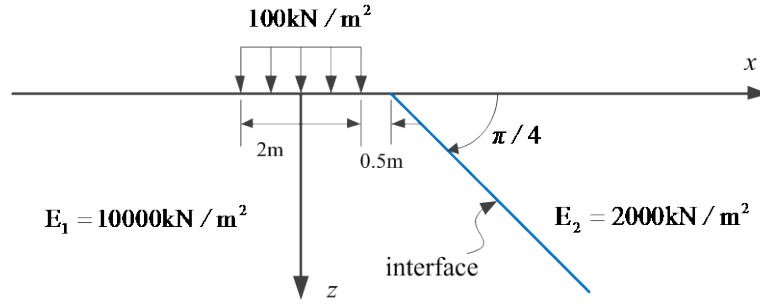
Fig. 8. Bi-material elastic halfspace with an inclined interface plane and subjected to normal

pressure over a square area on the horizontal boundary surface ($v_1 = v_2 = 0$)
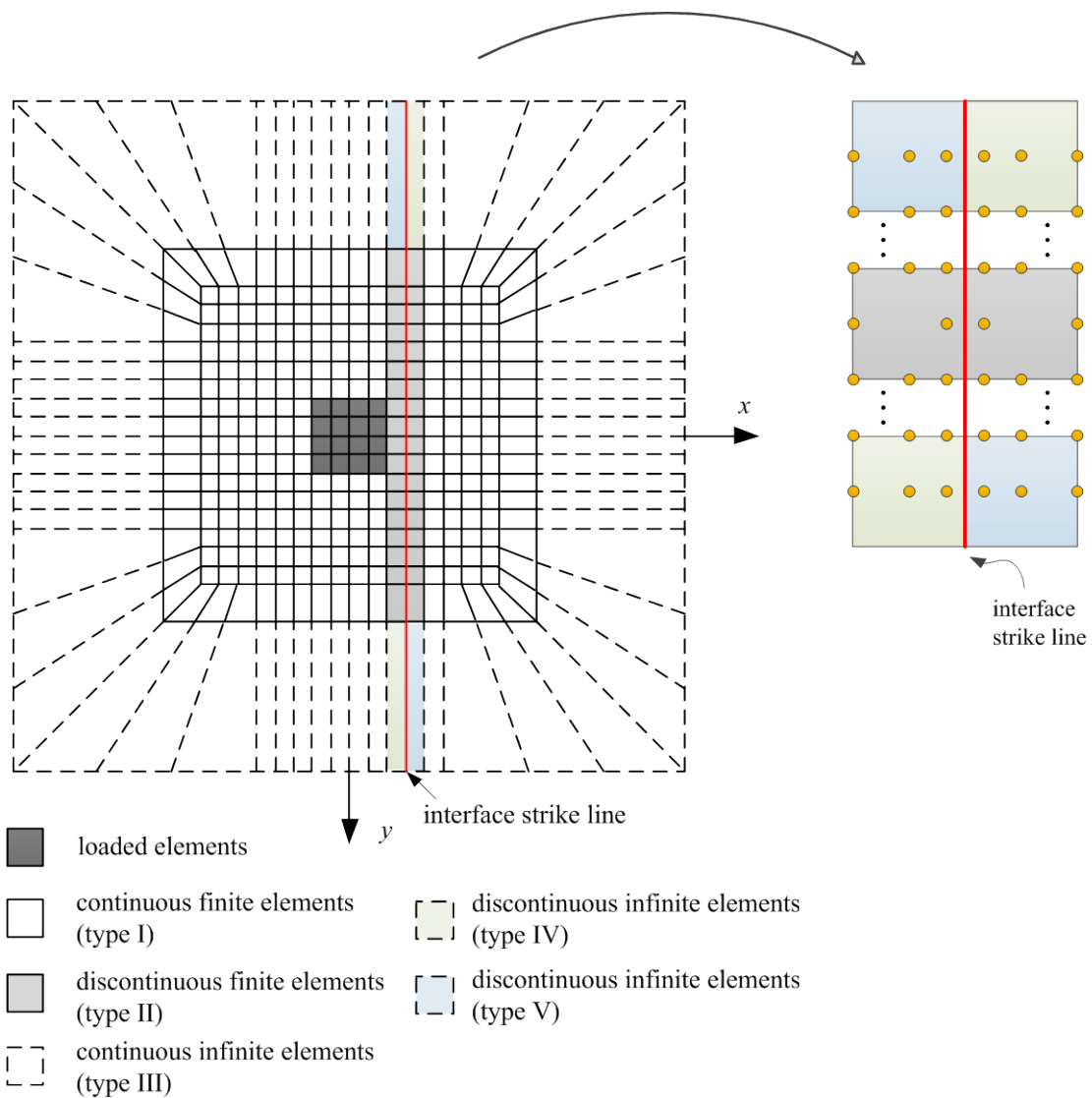
Fig. 9. The boundary mesh on the boundary surface with 1192 nodes for 284 finite continuous

elements (I), 36 finite discontinuous elements (II), 60 infinite continuous elements (III) and 4

infinite discontinuous elements (2 for IV and 2 for V)
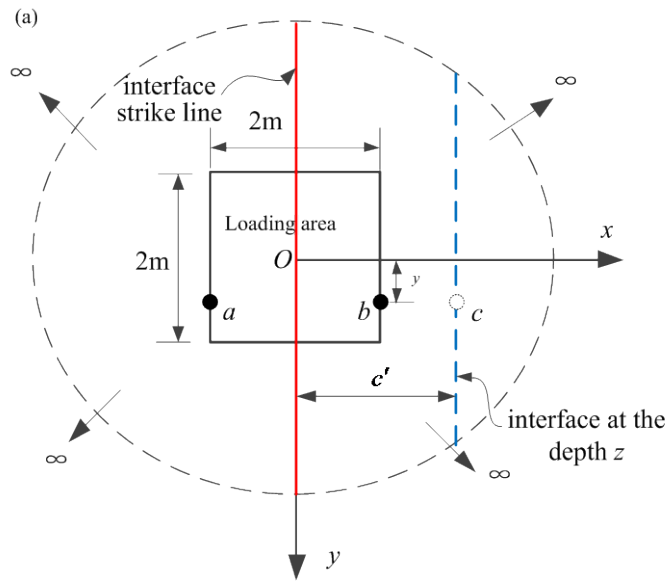
(10a) horizontal boundary surface
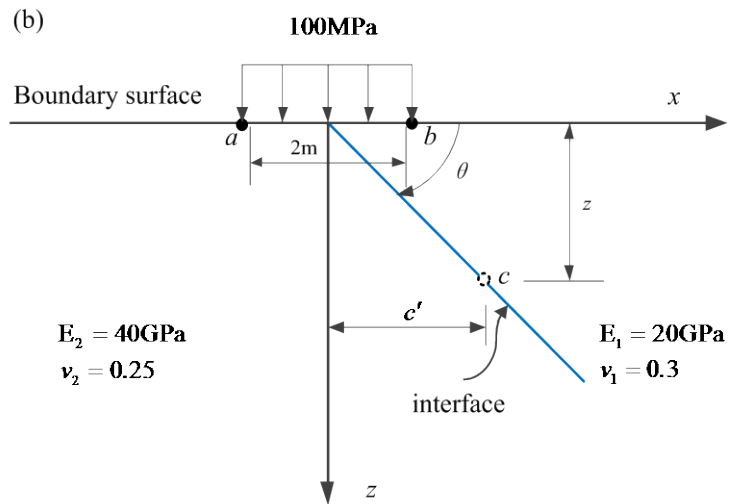
(10b) vertical cross-section

Fig. 10. A square footing acting on the strike line area of a bi-material elastic halfspace with an arbitrarily inclined interface plane
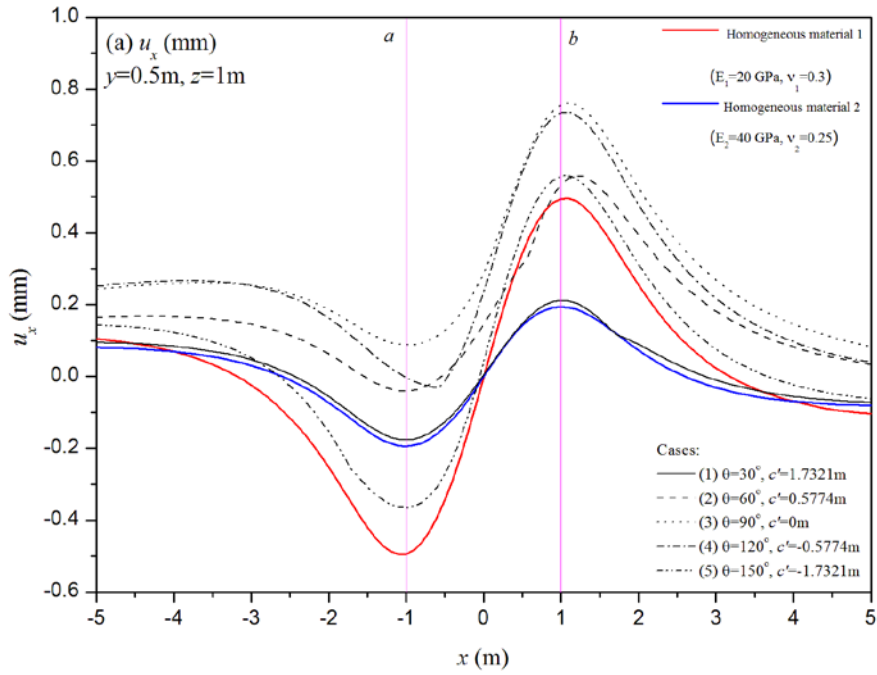
(11a) displacement u_x
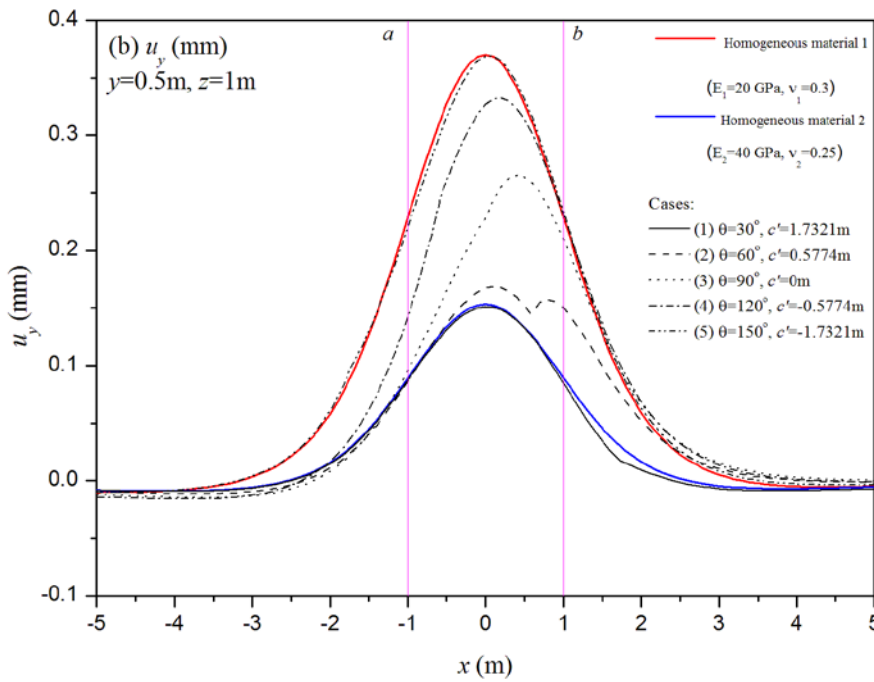
(11b) displacement u_y
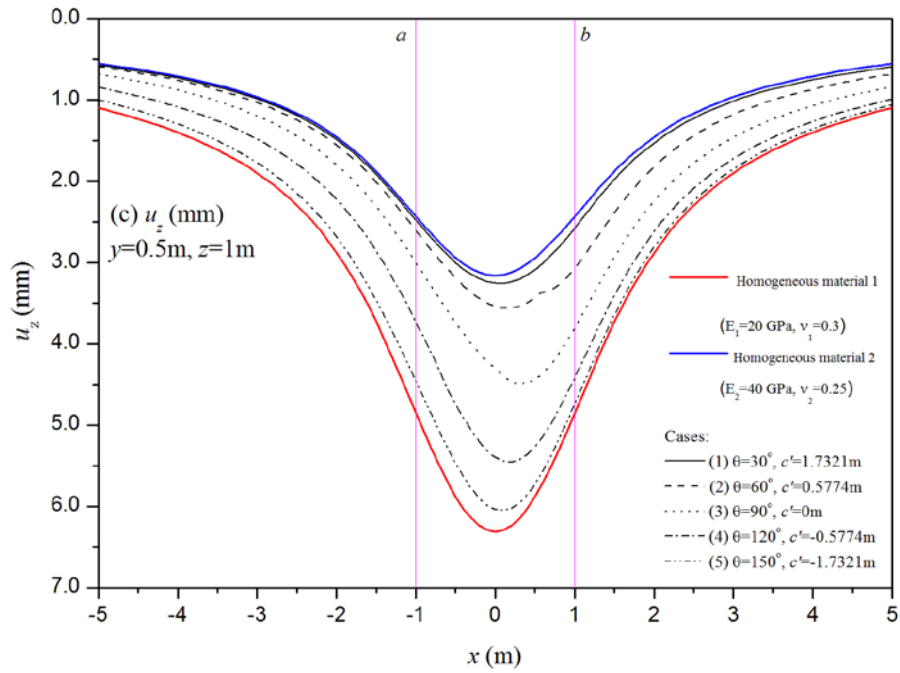
(11c) displacement u_z

Fig. 11. Variation of three displacement components (y=0.5 m and z=1 m)
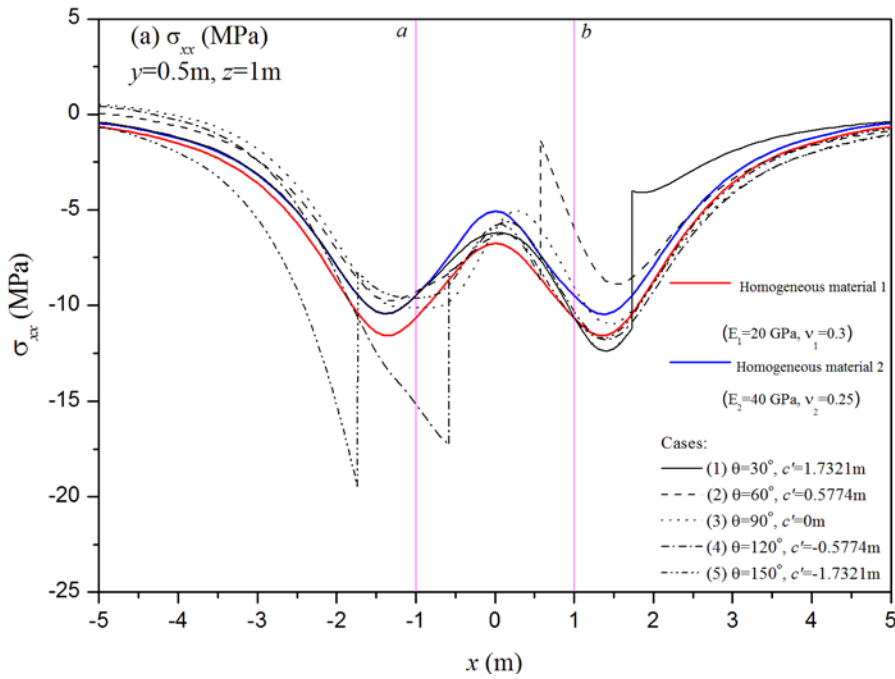
(12a) stress σ_{xx}
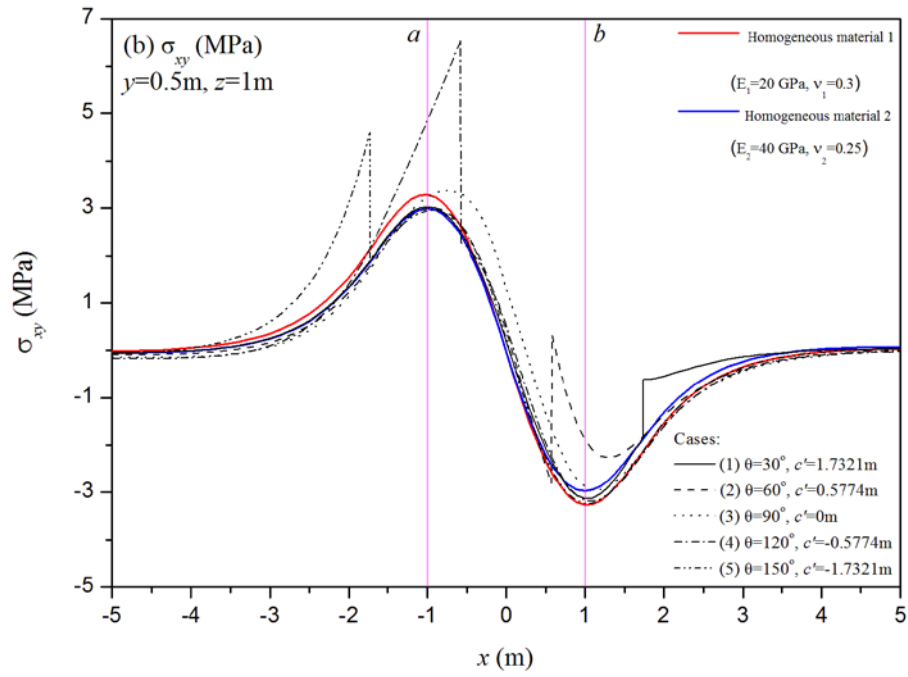
(12b) stress σ_{xy}
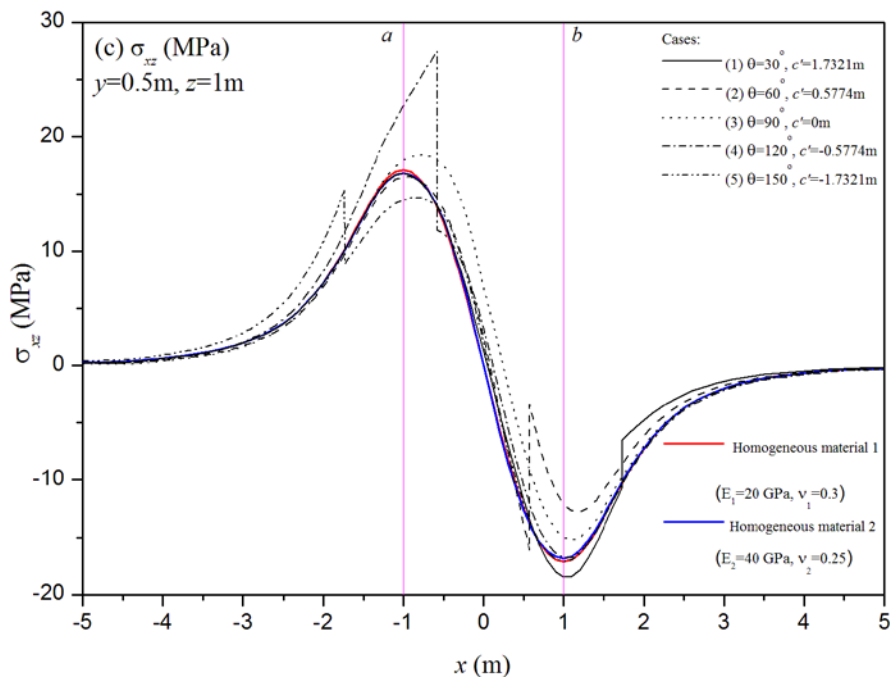
(12c) stress σ_{xz}
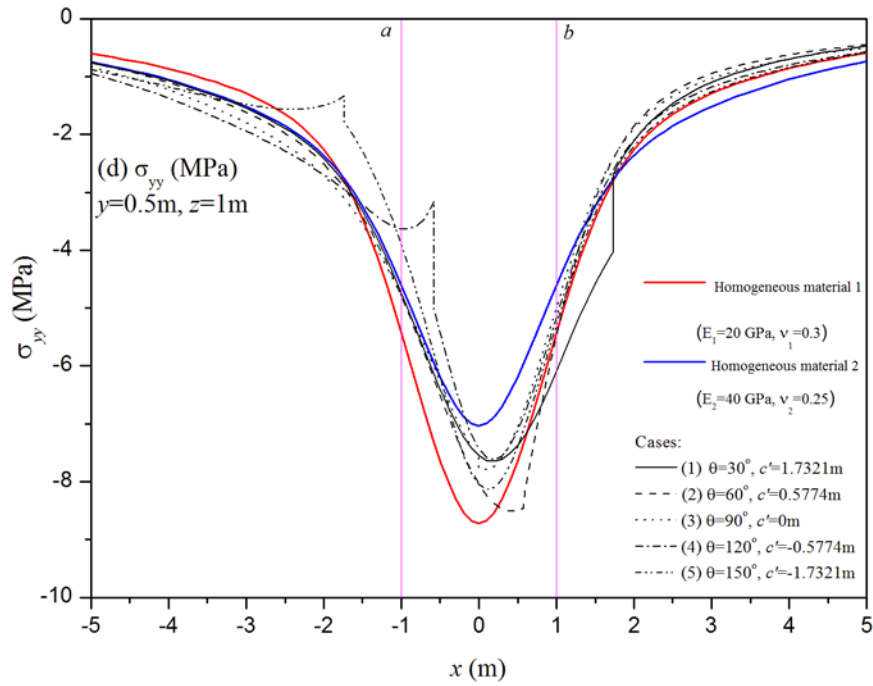
(12d) stress σ_yy
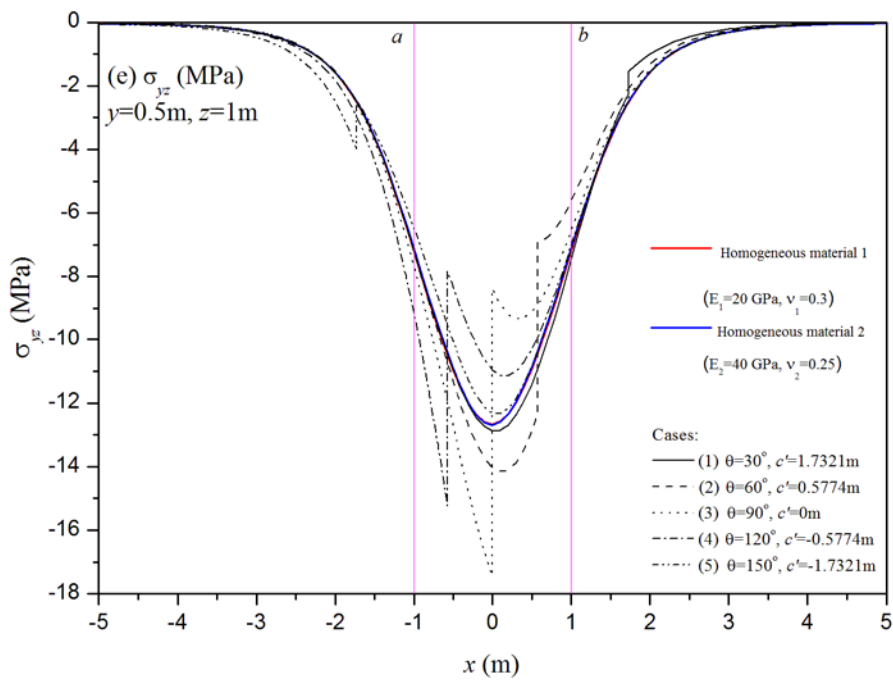
(12e) stress σ_yz
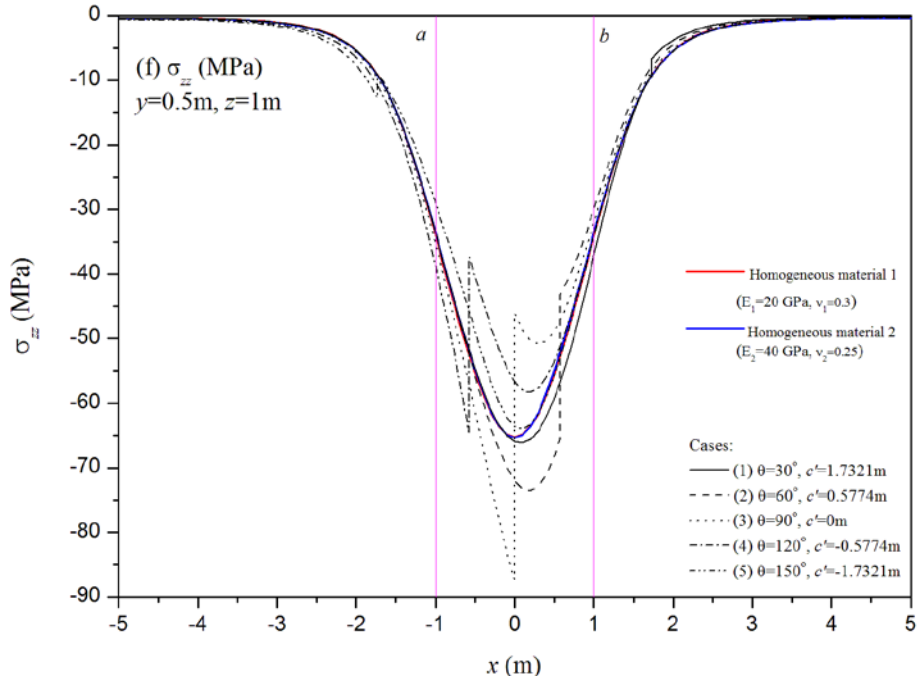
(12f) stress σ_{zz}

Fig. 12. Variation of stress components (y=0.5 m and z=1 m)
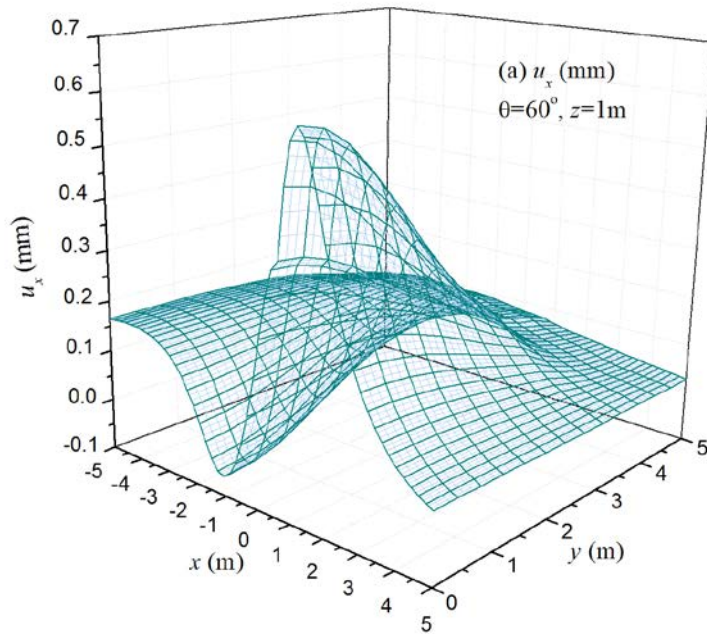
(13a) displacement u_x
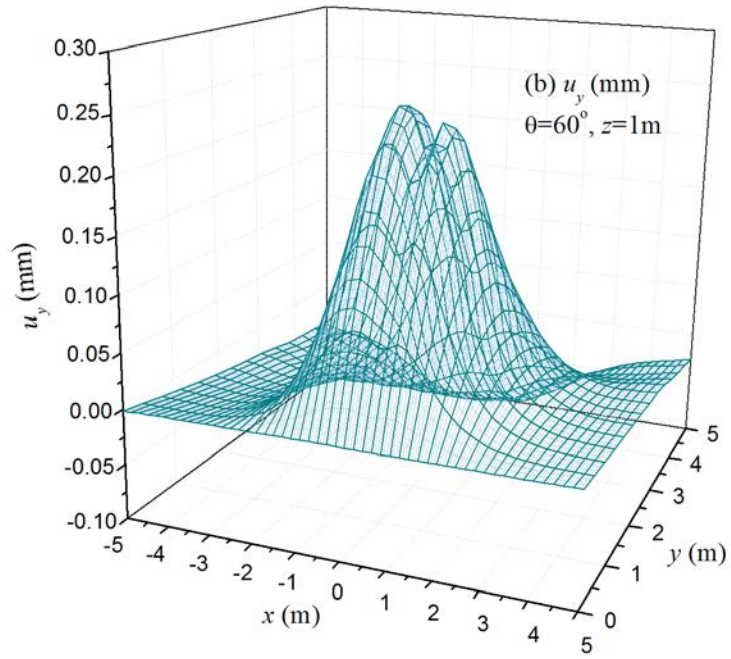
(13b) displacement u_y
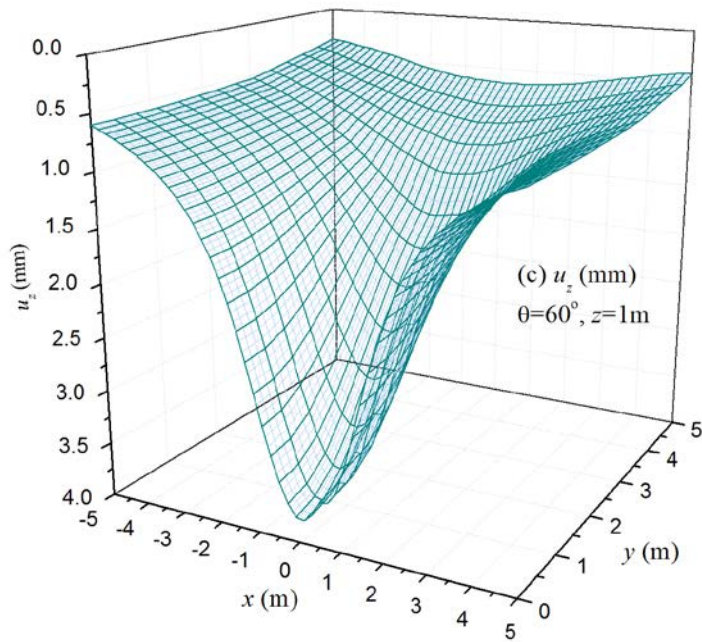
(13c) displacement u_z

Fig.13. Variation of displacements with the horizontal distance y
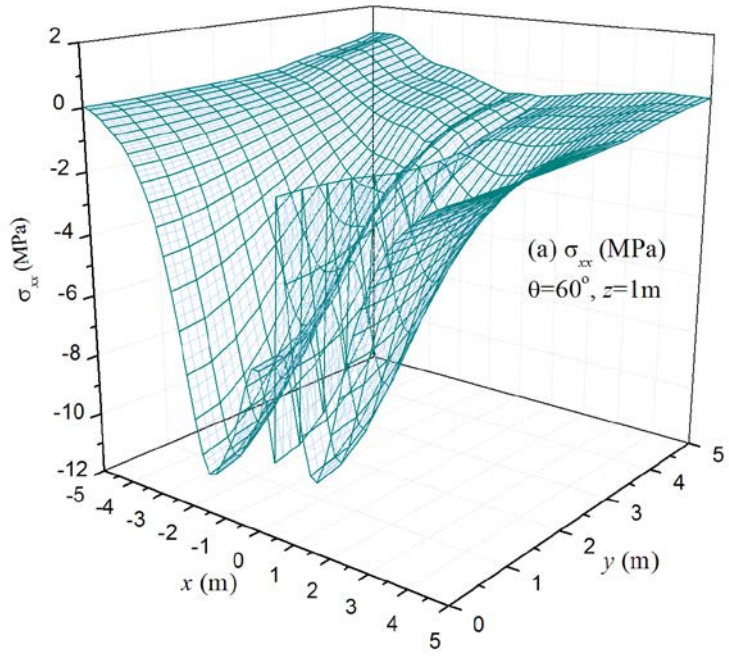
(14a) stress σ$_{xx}$
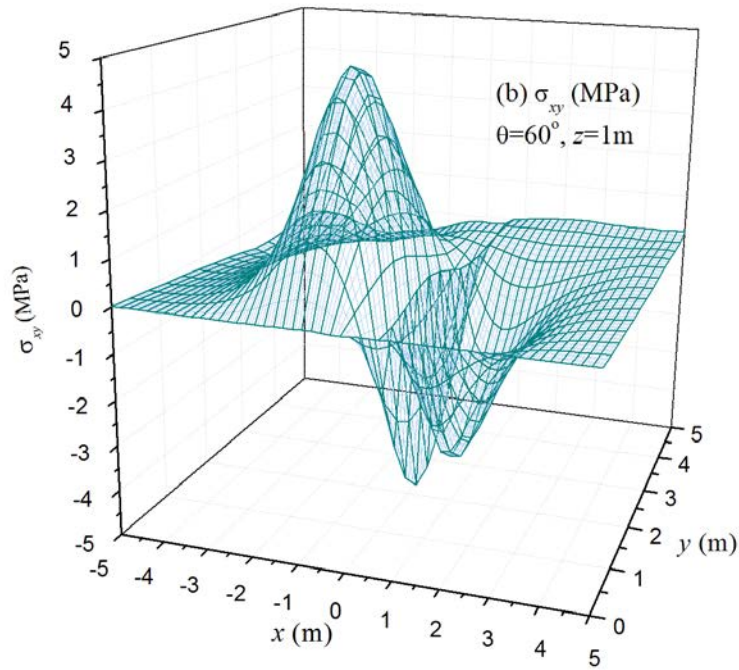
(14b) stress σ$_{xy}$
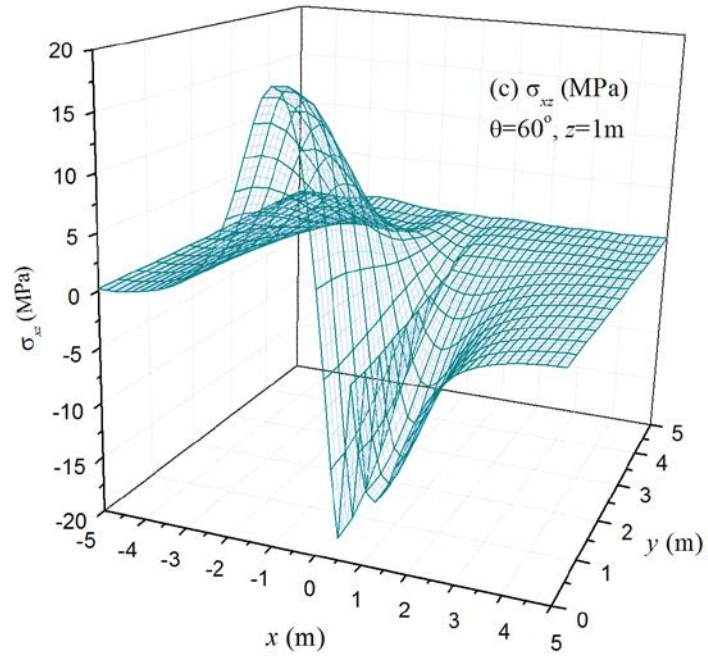
(14c) stress σ_{xz}
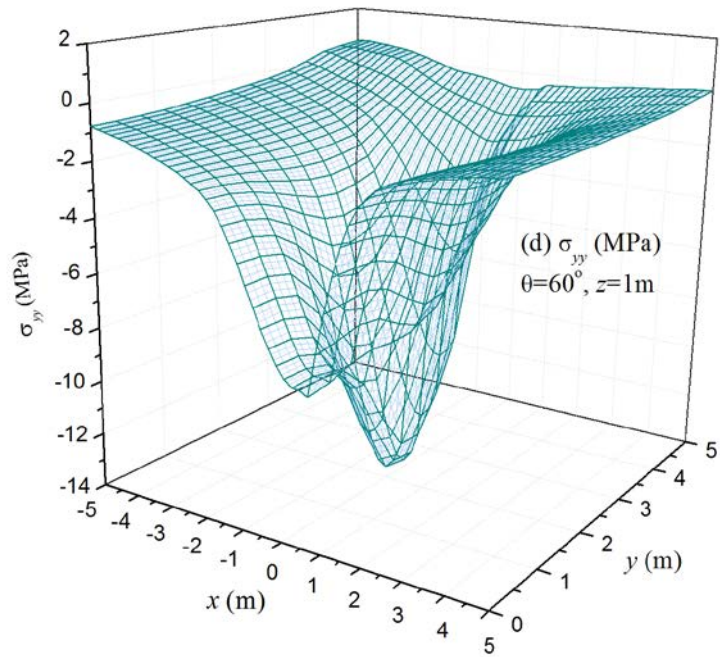
(14d) stress σ_{yy}
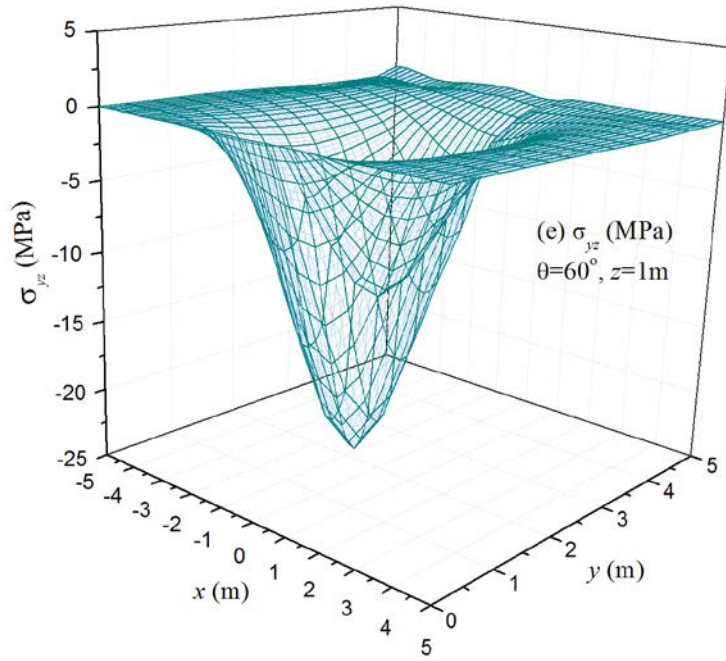
(14e) stress σ_{yz}
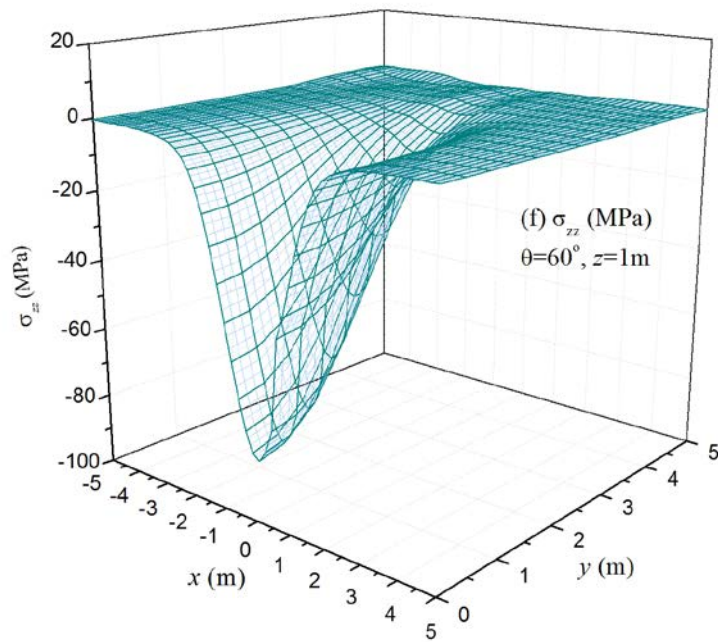
(14f) stress σ_{zz}

Fig. 14. Variation of stresses with the horizontal distance y ($\theta=60^{\circ}$, $z=1$m)
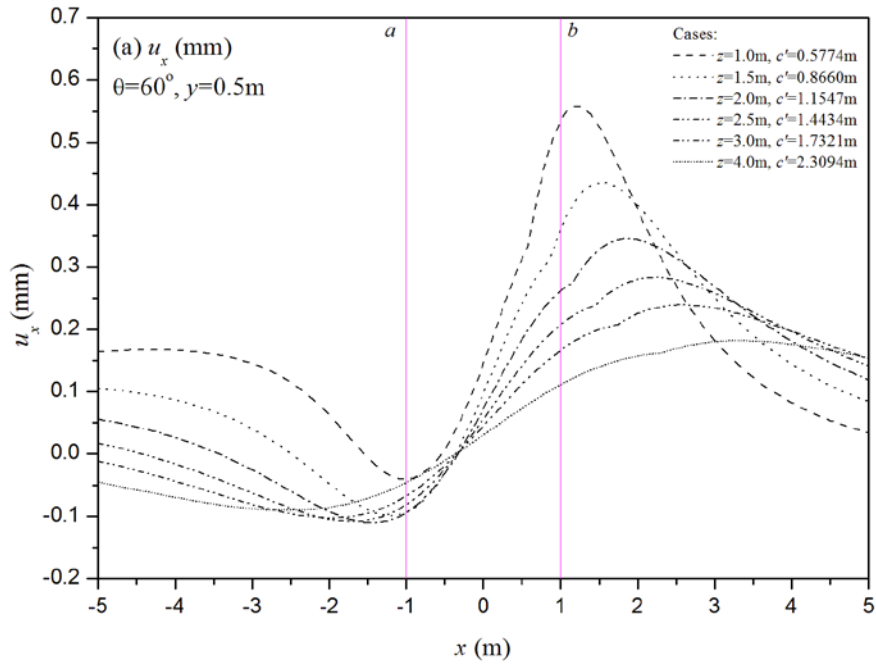
(15a) displacement u_x
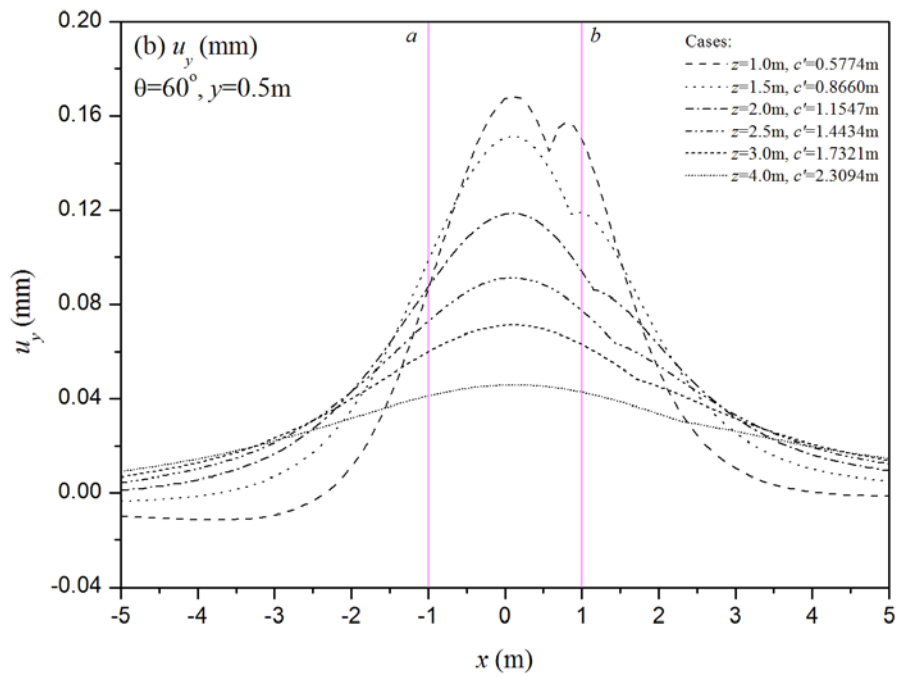
(15b) displacement u_y
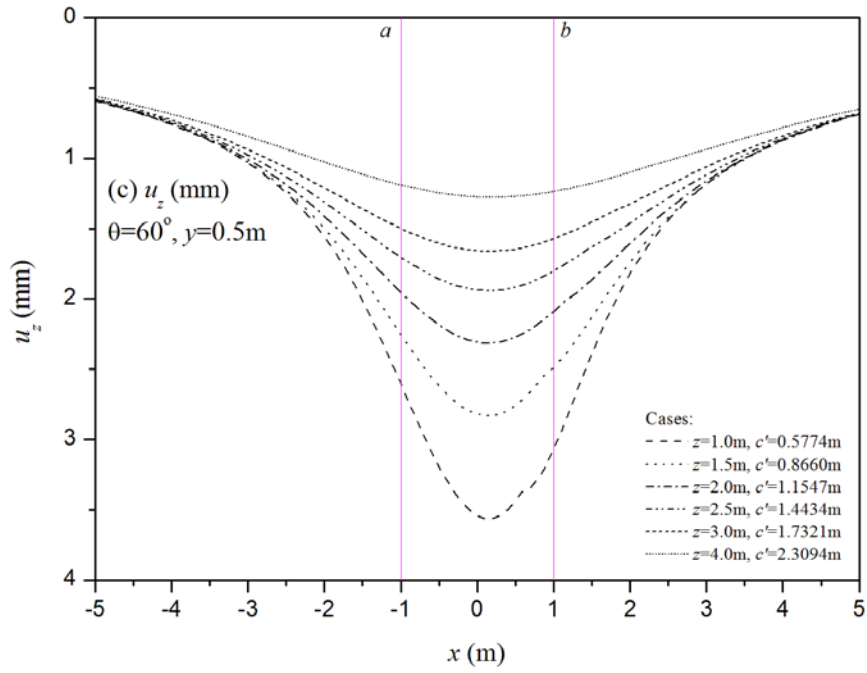
(15c) displacement u_z

Fig. 15. Variation of displacements with the depth z ($\theta=60°$, $y=0.5$m)
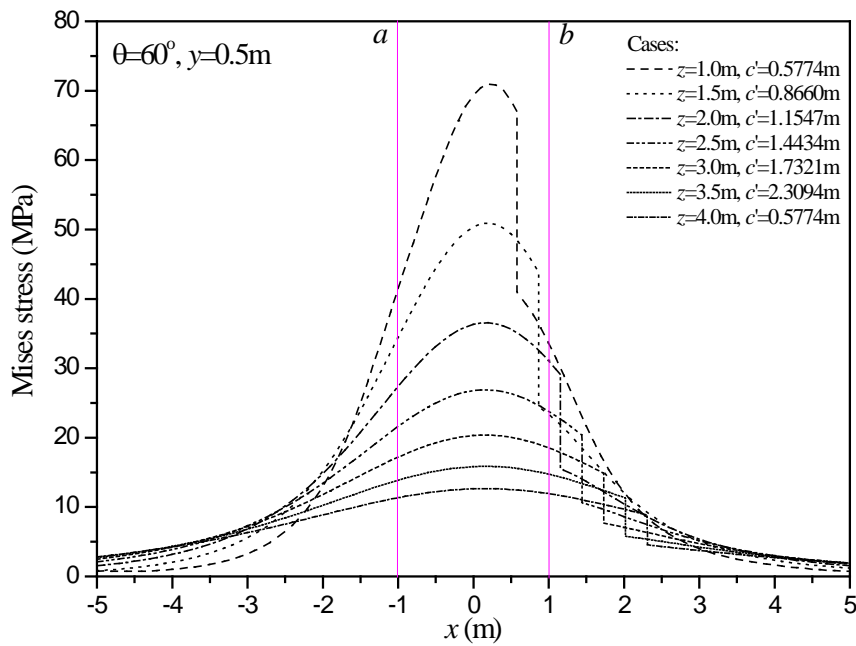
Fig. 16. Variation of Mises stress with the depth z ($\theta=60°$, $y=0.5$m)
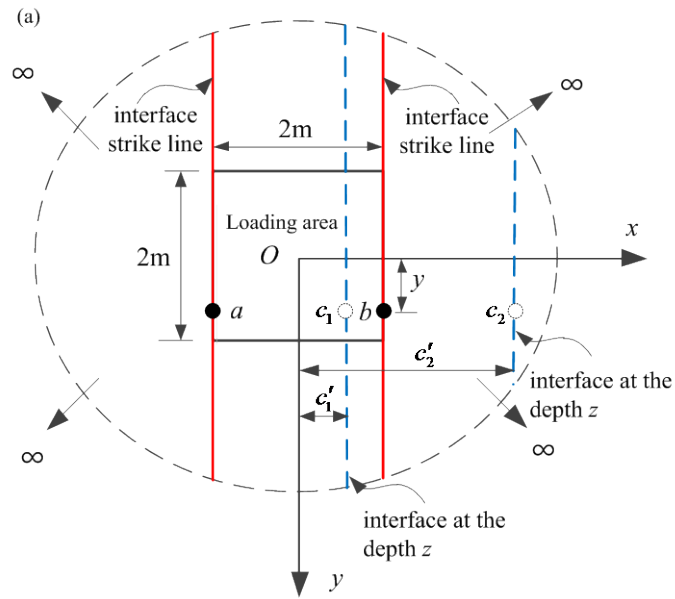
(17a) horizontal boundary surface
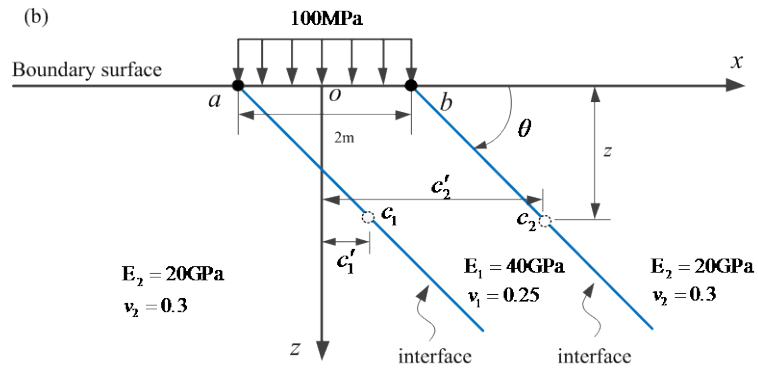
(17b) vertical cross-section

Fig. 17. Square footing on three-material halfspace with two non-horizontally placed and parallel interfaces
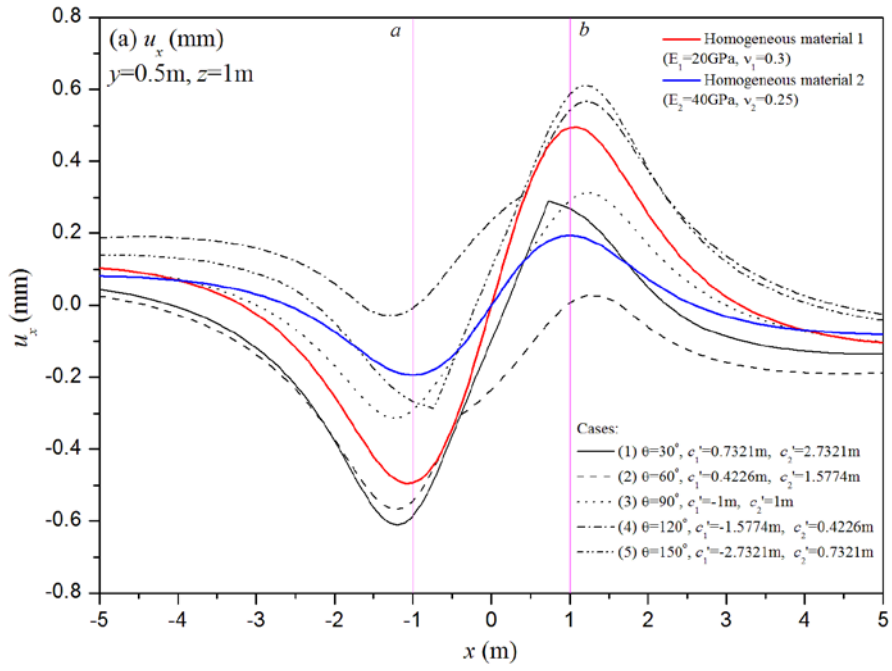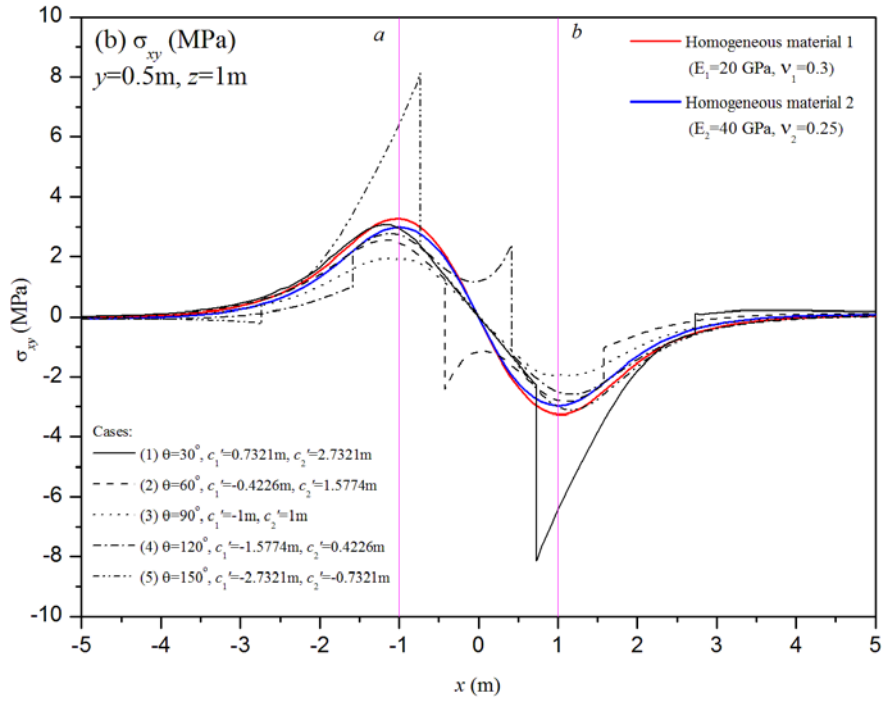
(18a) displacement u_x
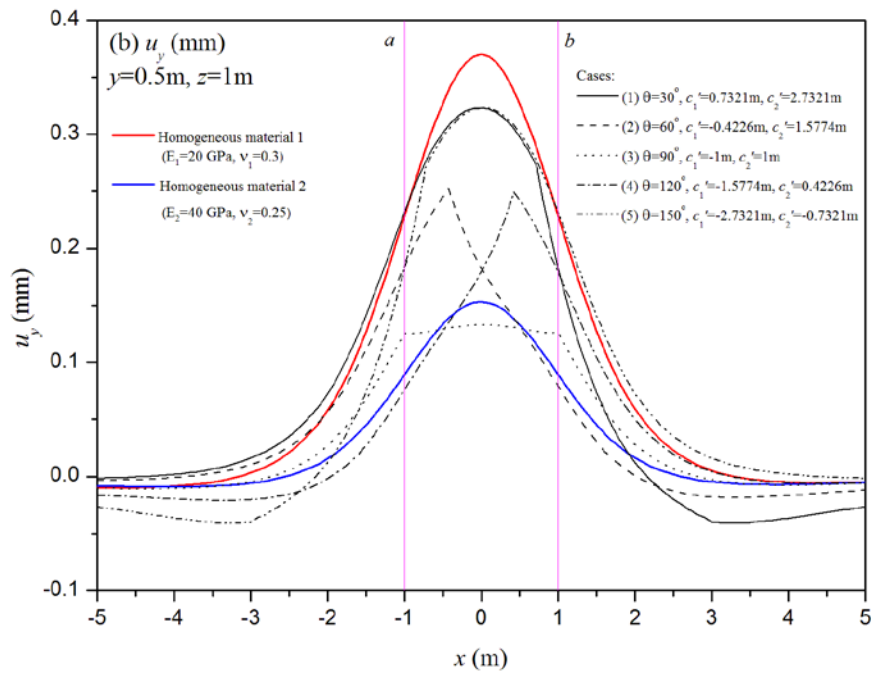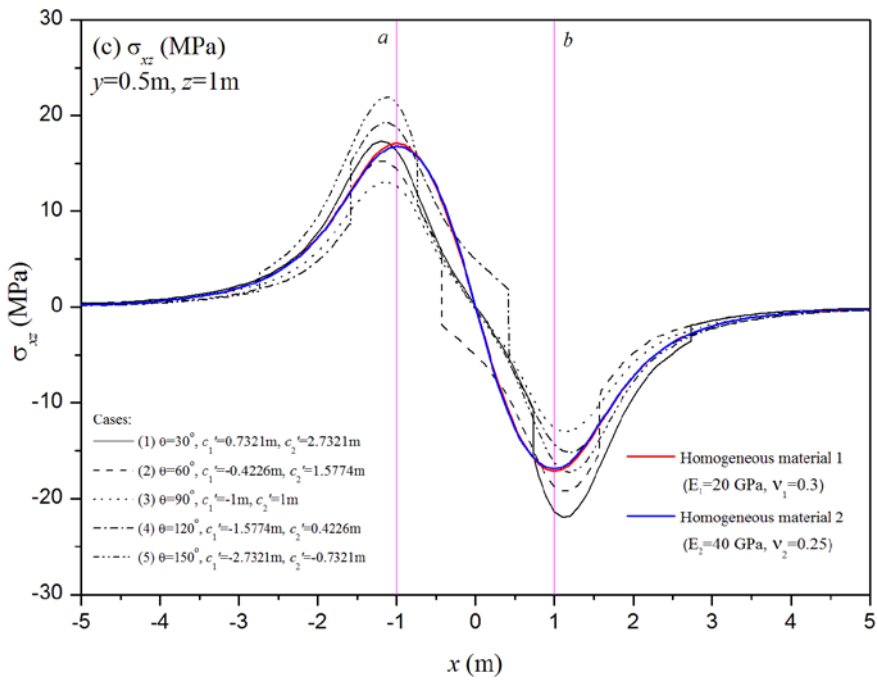

(18b) displacement u_y
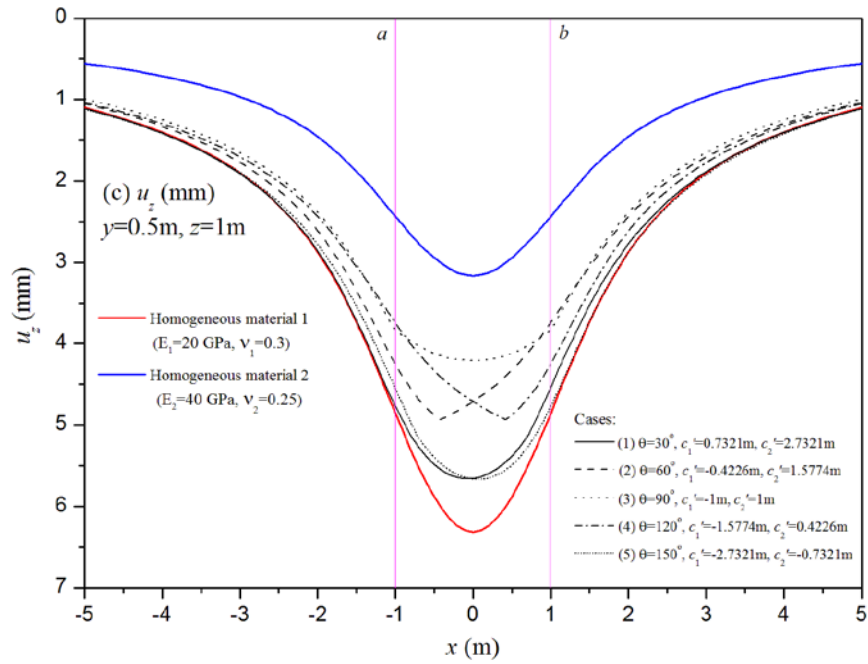
(18c) displacement u_z

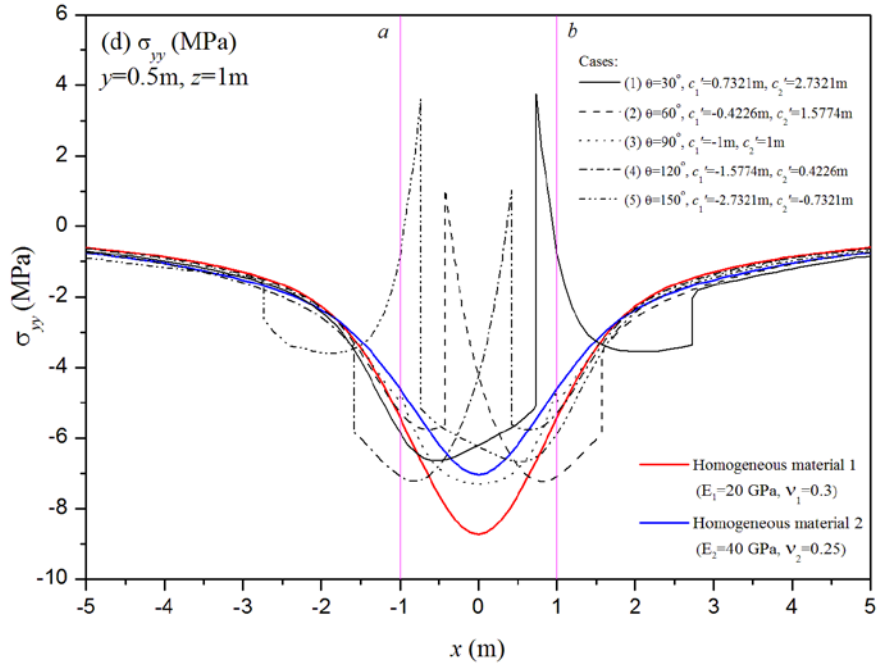Fig. 18. Variation of three displacement components with the angle θ (y=0.5m and z=1m)
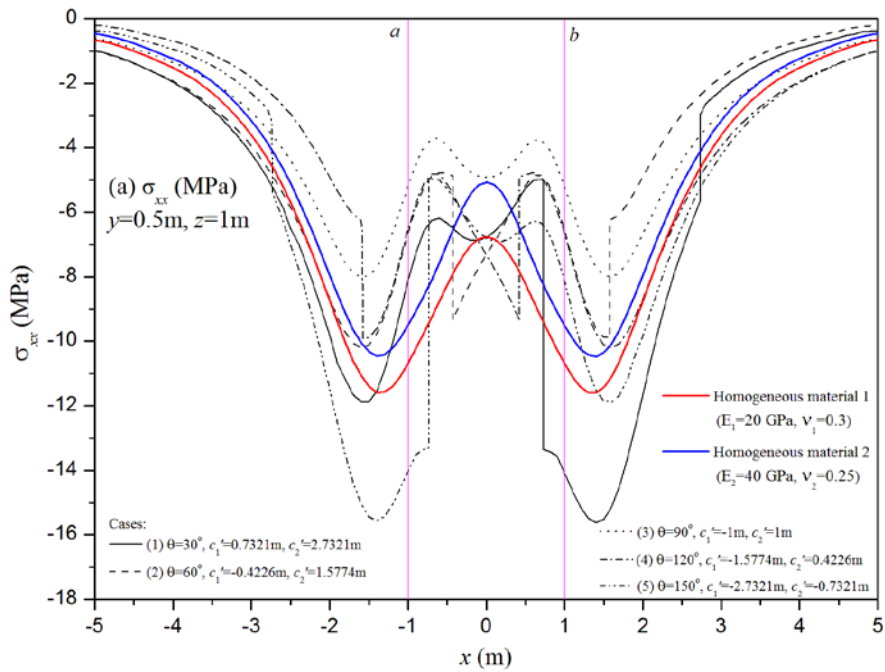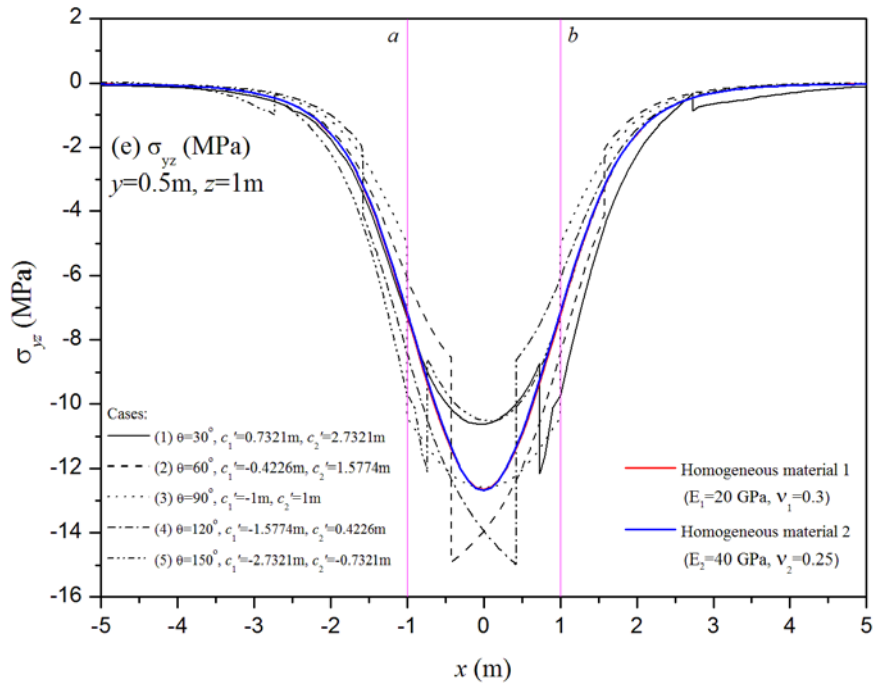

(19a) stress σ_{xx}

(19b) stress σ_{xy}

(19c) stress σ_{xz}

(19d) stress σ_{yy}

(19e) stress σ_{yz}
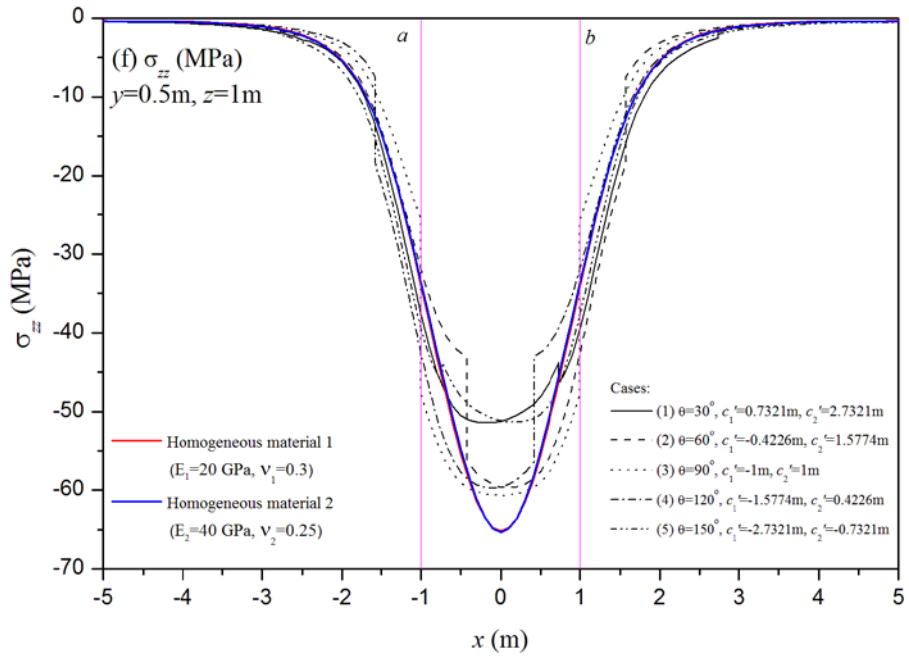
(19f) stress σ_{zz}

Fig. 19. Variation of six stress components with the angle θ (y=0.5m and z=1m)

Stress jump	θ (°)	bi-material halfspace	three-material halfspace	
		$x = c'$	$x = c_1'$	$x = c_2'$
$\Delta\sigma_{xx}$	30	7.1754	8.3462	2.6803
	60	7.3931	4.4729	3.9206
	90	0.0009	0.0007	0.0006
	120	9.0623	3.3704	4.4491
	150	11.2755	2.1995	8.2961
$\Delta\sigma_{xy}$	30	1.2214	5.8617	0.6966
	60	3.1317	3.6639	1.2041
	90	0.0002	0.0001	0.0009
	120	4.2760	1.2354	3.6809
	150	2.6902	0.8616	5.8195
$\Delta\sigma_{xz}$	30	4.1517	4.9881	1.7107
	60	12.7937	7.7645	5.9670
	90	0.0005	0.0002	0.0003
	120	15.6937	6.5093	7.7229
	150	6.5013	1.9526	4.9945
$\Delta\sigma_{yy}$	30	1.3539	8.8661	1.3316
	60	0.1489	6.6653	2.1390
	90	0.1862	0.3373	0.3216
	120	1.8660	2.5628	6.6584
	150	0.4631	0.9038	8.7963
$\Delta\sigma_{yz}$	30	0.7079	3.4214	0.5584
	60	5.4388	6.3572	2.4775
	90	9.0441	5.4129	5.4097
	120	7.3972	1.9396	6.3861
	150	1.5502	0.9062	3.4983
$\Delta\sigma_{zz}$	30	2.4086	2.5032	0.8887
	60	22.2426	13.4394	10.9973
	90	41.1799	22.0673	22.0424
	120	27.1359	10.9521	13.3676
	150	3.7430	0.2147	2.3860